Inverting Glacial Isostatic Adjustment signal using Bayesian framework and two linearly relaxing rheologies

L. Caron, L. Métivier, M. Greff-Lefftz, L. Fleitout, H. Rouby

Geophysical Journal International

Geophys. J. Int. (2017) **209,** 1126–1147
Advance Access publication 2017 February 27
GJI Gravity, geodesy and tides

doi: 10.1093/gji/ggx083

Inverting Glacial Isostatic Adjustment signal using Bayesian framework and two linearly relaxing rheologies

L. Caron,[1,*] L. Métivier,[2] M. Greff-Lefftz,[1] L. Fleitout[3] and H. Rouby[2]

[1]*Institut de Physique du Globe de Paris, Sorbonne Paris Cité, Université Paris Diderot UMR* 7154 *CNRS,* 1 *rue Jussieu, F-*75238 *Paris Cedex* 05*, France. E-mail: caron@ipgp.fr*
[2]*Institut Géographique National, LAREG,* 6-8 *Avenue Blaise Pascal, F-*77455 *Marne-la-Vallée, France*
[3]*Ecole Normale Supérieure and CNRS* UMR8538*, PSL Research University, F-*75005 *Paris, France*

Accepted 2017 February 25. Received 2017 February 18; in original form 2015 September 29

SUMMARY

Glacial Isostatic Adjustment (GIA) models commonly assume a mantle with a viscoelastic Maxwell rheology and a fixed ice history model. Here, we use a Bayesian Monte Carlo approach with a Markov chain formalism to invert the global GIA signal simultaneously for the mechanical properties of the mantle and the volumes of the ice sheets, using as starting ice models two previously published ice histories. Two stress relaxing rheologies are considered: Burgers and Maxwell linear viscoelasticities. A total of 5720 global palaeo sea level records are used, covering the last 35 kyr. Our goal is not only to seek the model best fitting this data set, but also to determine and display the range of possible solutions with their respective probability of explaining the data. In all cases, our *a posteriori* probability maps exhibit the classic character of solutions for GIA-determined mantle viscosity with two distinct peaks. What is new in our treatment is the presence of the bi-viscous Burgers rheology and the fact that we invert rheology jointly with ice history, in combination with the greatly expanded palaeo sea level records. The solutions tend to be characterized by an upper-mantle viscosity of around 5×10^{20} Pa s with one preferred lower-mantle viscosities at 3×10^{21} Pa s and the other more than 2×10^{22} Pa s, a rather classical pairing. Best-fitting models depend upon the starting ice history and the stress relaxing law. A first peak (P1) has the highest probability only in the case with a Maxwell rheology and ice history based on ICE-5G, while the second peak (P2) is favoured for ANU-based ice history or Burgers stress relaxation. The latter solution also may satisfy lower-mantle viscosity inferences from long-term geodynamics and gravity gradient anomalies over Laurentia. P2 is also consistent with large Laurentian and Fennoscandian ice-sheet volumes at the Last Glacial Maximum (LGM) and smaller LGM Antarctic ice volume than in either ICE-5G or ANU. Exploration of a bi-viscous linear relaxing rheology in GIA now seems logical due to a new set of requirements to satisfy observations of transient post-seismic flow seen so ubiquitously in space gravimetry and other global geodetic data.

Key words: Gravity anomalies and Earth structure; Sea level change; Transient deformation; Probability distributions; Dynamics of lithosphere and mantle; Rheology: mantle.

1 INTRODUCTION

During glacial cycles, redistribution of the ice and oceanic water masses at the Earth surface causes gravitational perturbations and deformations in the lithosphere and mantle. This phenomenon, called Glacial Isostatic Adjustment (GIA), is controlled by ice loading history, buoyancy forces and the Earth's rheology.

Considering that the time scale of GIA is long enough to allow creep to occur in mantle rocks, a mathematically tractable model approximation for the mantle constitutive law is the linear viscoelastic model of a Maxwell body (Peltier 1974; Mitrovica & Forte 2004; Lambeck *et al.* 2010, 2014). When a deviatoric stress is instantaneously applied and held constant, a Maxwell material exhibits an instantaneous elastic strain followed by a constant strain rate that is exactly the same as the response of a Newtonian viscous fluid. While the elastic parameters can be estimated via seismological and laboratory studies, the value of the viscosity is elusive. In particular, disagreements exist over the viscosity increase between

* Now at: Jet Propulsion Laboratory – California Institute of technology, 4800 Oak Grove Drive MS 300-323, Pasadena, CA 91109-8099, USA.

upper mantle and lower mantle. GIA inversions at the global scale can be roughly classified into two groups: one features a moderate increase of, at most, one order of magnitude (e.g. Peltier 2004; Paulson *et al.* 2007; Peltier & Drummond 2008; Geruo *et al.* 2013), or a much higher viscosity increase, from one and a half to two orders of magnitude (Lambeck 1990; Lambeck *et al.* 2010, 2014). The existence of the contrasting pair of viscosity solutions using GIA data has long been recognized (O'Connell 1971), and the distinction between these two classes of GIA models that are realized from the solutions is quite important. For example, the class of models featuring a relatively smaller viscosity increase is employed for correcting the trend caused by GIA that is present in time-varying space gravimetry, where trends in hydrology, ice sheet or ocean mass is sought (see GRACE Tellus solutions, from e.g. Chambers & Bonin 2012; Watkins *et al.* 2015, or in the IPPC last assessment in Church *et al.* 2013). The alternative class of solutions (with higher increases in viscosity between upper mantle and lower mantle), however, exhibits greater consistency with solutions based on mantle convection models that employ global seismic anomalies, geoid and surface plate motion data for parameterization and analyses (Hager *et al.* 1984; Forte & Peltier 1991; Ricard *et al.* 1993; Ivins *et al.* 1993; Čadek & Fleitout 2003; Steinberger & Calderwood 2006; Greff-Lefftz *et al.* 2016).

A possible resolution of this dilemma is that GIA and mantle convection have very different time and length scales. While Forte & Mitrovica (1996), Mitrovica & Forte (1997), Mitrovica & Forte (2004) and Kaufmann & Lambeck (2002) have demonstrated that it is possible to reconcile these through joint inversions using the Maxwell rheology, it is also possible that the viscosity will differ because of the contrasting time scales involved.

Indeed, various factors such as temperature, grain-size, water content or mineral structure and composition induce heterogeneities at various scales in the mantle viscosity. The mantle can be considered as a mixture of materials of different viscosities. Self-consistent homogenization theory (Ivins & Sammis 1996) and creep experiments on multiphase rocks (Ji & Zhao 1993, 1994) show that a mix of two Maxwell materials with different viscosities exhibits a transient rapid relaxation before reaching a steady strain rate, that is, a constant apparent viscosity. The amplitude of the transient relaxation is predicted to increase when several scales of heterogeneities are superimposed. Thus, it seems relevant to investigate what could be the role of transient creep in the GIA signal. Such heterogeneity has recently been advocated for the lower mantle by the fact that the two phases of perovskite (MgO and SiO_3) have quite different intrinsic susceptibility to creep (Marquardt & Miyagi 2015).

Further evidence of more complex behaviour than described by a Maxwell material comes from the laboratory, where tertiary creep is ubiquitous. Peltier *et al.* (1980) recognized the possibility of tertiary creep as an alternative constitutive framework for mantle response to glacial unloading and tested the response of a model involving a standard linear solid relaxation time advocated by Anderson & Minster (1979) to the Hudson Bay free decay spectra, showing that the more complex rheology poorly fit these data.

The test, however, was limited in both scope of the parameters examined and the pertinent space and time of the data set. Subsequently, Yuen *et al.* (1986) found that by introducing a close relative of the Maxwell body, a four parameter linear stress relaxing material called Burgers rheology, light might be shed on the dilemma of having both a reduced and an elevated lower-mantle viscosity operating on GIA and convective time scales, respectively. The principal ingredient of a Burgers rheology in the lower mantle is that it allowed deformation to be controlled by two viscosities, thus inherently having the capacity to explain GIA and convective based inferences of viscosity. Extensive studies of Burgers rheology as a model for GIA have remained rather limited, in part due to the elusiveness of incorporating high temperature and pressure laboratory data from rock deformation experiments.

The re-emergence of the Burgers fluid constitutive assumption for describing upper-mantle flow has been necessitated by geodetic observations (GNSS and GRACE) following the great earthquakes of the past decade (Pollitz 2005; Melini *et al.* 2008; Han *et al.* 2008; Panet *et al.* 2010; Trubienko *et al.* 2013; Meade *et al.* 2013). It seems quite logical now to re-examine the constitutive assumption as applied to the GIA model predictions, especially in light of the more than one order of magnitude increase in the amount of RSL data currently available compared to the 1990's (Tushingham & Peltier 1992).

A key contributor to the GIA signal is the ice loading history. The load history in the standard GIA theory requires proper representation of ice thickness change over time and location at the Earth's surface. While only grounded ice, or marine ice that sits above flotation, loads the solid Earth as a part of this history, there is also an important meltwater redistribution to the global oceans.

It is important to note that palaeoclimatic and geological indicators (e.g. moraine deposits) from field-based work (e.g. Dyke & Prest 1987; Clark *et al.* 2004; Svendsen *et al.* 2004) provide key information for reconstructing the ice sheet extent over time. Numerical models coupled to past climatology, oceanography and ice-sheet dynamics (e.g. Zweck & Huybrechts 2005; Charbit *et al.* 2007; Beghin *et al.* 2014) provide some additional insights on the time-evolution of ice sheets. However, it is very difficult to bring this information together to constrain past ice thickness and, therefore, volume. Uncertainty in ice history, especially as it affects inferences about volume, is a major challenge in GIA models.

Previous publications have demonstrated that powerful estimations of the mantle viscosity can be obtained in specific locations of the globe with minimal influence from ice loading history. These studies rely on using differential sea level highstands (Lambeck & Nakada 1990; Bradley *et al.* 2016), relaxation spectra (McConnell 1968; Parsons 1972; Mitrovica & Peltier 1993a; Martinec & Wolf 2005) and post-glacial decay times (Mitrovica & Peltier 1993b; Mitrovica & Forte 2004). In particular, these studies allow upper-mantle viscosity values to be constrained to 2–3×10^{20} Pa s in the Australian region and to less than 1.5×10^{20} Pa s in South East Asia using sea level highstands. In addition, constraints are about 3–6×10^{20} Pa s in Fennoscandia using relaxation spectra and decay times, and to about 10^{21} Pa s in the Laurentia region, based on decay times for the same depths in the upper mantle. Other data sets, such as palaeo sea level measurement, provide complementary information by sampling GIA signal on a global spatial distribution, which extends the sensitivity of GIA to viscosity deeper in the mantle (due to larger spatial scales of the samples), and to account for a more global viscosity estimate. In this study we propose to use a global relative sea level (RSL) data set, consisting of 5720 records, to acquire information about both mantle viscosity and ice loading history. One problem with RSL data is that model inferences are influenced by their sensitivity to both the space-time history of the ice load and mantle rheology. Indeed, when comparing the two most emblematic global GIA models (Peltier 2004; Lambeck *et al.* 2014), we notice that they are different in terms of both load amplitude and timing. Furthermore, they differ in total ice mass at the Last Glacial Maximum (LGM), and in mass distribution among continental and marine-based ice sheets. Our rather humble goal is to illustrate how the information from RSL data

constraining ice history and mantle viscosity are coupled in these two global models, and to show how this coupling is never really disentangled, although here we make an extensive effort to do so. To this end, we employ a Bayesian method that allows us to explore the parameter space and reveal the trade-offs, uncertainty and other non-uniquenesses inherent to GIA solutions.

This paper is organized as follows: in Section 2, we present the calculation methods as well as the model setting. In Section 3, we describe the inversion results coupling Maxwell and Burgers rheologies with ice models derived from the ANU and ICE-5G models. In Section 4, we discuss the implications of the results and, finally, we conclude in Section 5.

2 METHODS

2.1 Principle

We use loading Love numbers (Love 1909; Munk & MacDonald 1960; Longman 1962a,b; Farrell 1972), dependent on the stratification of the Earth in terms of density and rheological parameters, to represent the impulse response of the Earth to surface loading. Expanding the ice load with spherical harmonics, from degree one (Greff-Lefftz & Legros 1997) to 89, we can calculate surface displacements and geoid perturbations due to GIA. Instead of the commonly used viscoelastic normal modes approach (Peltier 1974), we use a Fourier transform method (Craig *et al.* 2016): for each frequency we solve the y_i system introduced by Alterman *et al.* (1959), expressing the Lamé parameters as a function of the frequency using the correspondence principle (Biot 1962). Note that using the Fourier transform makes the signal infinitely periodic, so our calculated deformation corresponds to the response to an infinite number of glacial cycles, as opposed to the normal mode approach with Laplace transform. Overall, we think this is an improvement as there were quite similar (although not identical) glacial cycles prior to the last one, which we can compute at no additional cost. Our method includes rotational feedback effect (Munk & MacDonald 1960; Han & Wahr 1989; Mitrovica *et al.* 2001) and the resolution of the sea level equation (Farrell & Clark 1976). Our method uses a simple fixed ocean-continent geometry which allows the GIA response to be perfectly linear with respect to the loading function, and thus to invert for ice history parameters via a linear least-squares algorithm. See the Appendix A1 for further details.

2.2 Calculation settings

The nominal mantle rheology used in GIA inversion is the linearly relaxing Maxwell viscoelastic model. It features an instantaneous elastic response followed by a viscous creep similar to a Newtonian fluid, and is represented in analogous mechanical diagram, in Fig. 1, by the association of a spring with Lamé coefficients λ_1 and μ_1, and a dashpot with viscosity 10^{η_1} in series. Note that we choose the viscosity parameters to be the logarithm of the actual viscosity value, as recommended by Mitrovica & Peltier (1991). Indeed, GIA signal is dependent on the logarithm of the viscosity, and the statistics (e.g. expected value or standard deviation) derived from it have to be consistent with this basic property. Burgers rheology is a linear viscoelastic model that exhibits the same features as Maxwell rheology with an additional transient relaxation. It is described by a Kelvin-Voigt body, that is, a dashpot element with viscosity 10^{η_2} (linked to the characteristic time scale of the transient response) in parallel with a spring element with shear modulus μ_2 (linked to the amplitude of the transient response), in series with a Maxwell body.

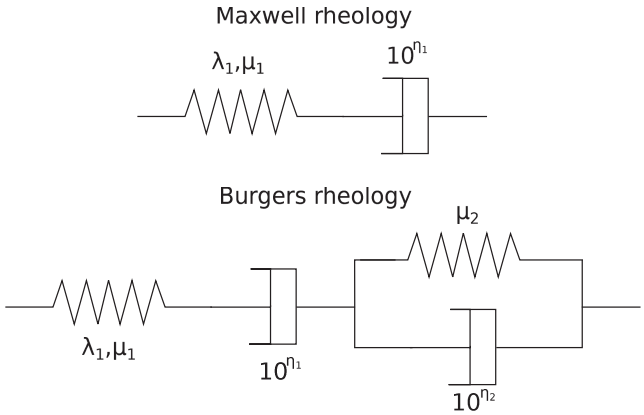

Figure 1. Mechanical diagram of Maxwell and Burgers rheologies.

We use a compressible layered Earth model with spherical symmetry. It describes the density and elastic moduli (λ_1 and μ_1) in radial profile, which are set to a volumetric average of the PREM Earth model (Dziewonski & Anderson 1981) for each layer, and the viscosity profile, the values for which we seek by inversion. The model features an elastic lithosphere with thickness T_e, a viscoelastic upper mantle with viscosity $10^{\eta_{\mathrm{UM}}}$, a viscoelastic lower mantle with viscosity $10^{\eta_{\mathrm{LM}}}$, a fluid outer core and a viscoelastic inner core. With Burgers rheology, we input additional ratios μ_1/μ_2 and $10^{\eta_1}/10^{\eta_2}$ that apply for the whole mantle. Of course, this is a simplification, as in reality the ratio could be different in each layer. Note that in the Burgers rheology case, $\eta_{\mathrm{UM},1}$ and $\eta_{\mathrm{UM},2}$ quantify long-term and transient viscosities, respectively, in the upper mantle, and the same applies to $\eta_{\mathrm{LM},1}$ and $\eta_{\mathrm{LM},2}$ notations in the lower mantle.

The ice model is obtained by regionally scaling the ice height of a reference model. We divide the model into West Laurentide (WL), East Laurentide (EL), Fennoscandia (F), Antarctica (A) and Greenland (G), and neglect the contribution of the mountain glaciers, thus avoiding ill-conditioned least square matrices. In each region the ice thickness is multiplied by a scalar coefficient α that applies for the whole glacial cycle, following Fleitout *et al.* (2006) (see Fig. 2 for notation and coverage of each ice region). Thus, we can adjust the mass distribution between the different ice sheets in the inversions. We also monitor the eustatic sea level at the LGM $\xi_{\mathrm{LGM}} = \sum_n \alpha_n V_n / S_{\mathrm{ocean}}$, where V_n is the ice volume change since the LGM in region n and S_{ocean} is the surface covered by oceans. Note that these coefficients only scale the change of ice thickness during the last glacial cycle (sole source of the GIA signal, along with the associated sea level change), yielding the actual ice thickness taken for computation: $H_{\mathrm{total}}(t,\theta,\varphi) = H_{\mathrm{present}}(t,\theta,\varphi) + \sum_n \alpha_n H_n^{\mathrm{ref}}(t,\theta,\varphi)$, with H_{present} the present-day ice thickness (non-zero in Antarctica and Greenland) and H_n^{ref} the ice thickness in region n provided by the reference ice model. For purposes of comparison, we test both the ANU (Lambeck *et al.* 2014) and ICE-5G (Peltier 2004) models as reference models.

2.3 Inverse method

We use Simulated Annealing (Kirkpatrick *et al.* 1983), a variation of the Monte Carlo with Markov chains method (Metropolis & Ulam 1949; Metropolis *et al.* 1953) to invert for η_{UM}, η_{LM}, T_e, $\log_{10}(\mu_1/\mu_2)$ and $\eta_1 - \eta_2$ (i.e. the logarithm of the viscosity ratio: $\log_{10}(10^{\eta_1}/10^{\eta_2})$. For a given Earth model with these parameters, we then invert for the α coefficients, applied to a given reference

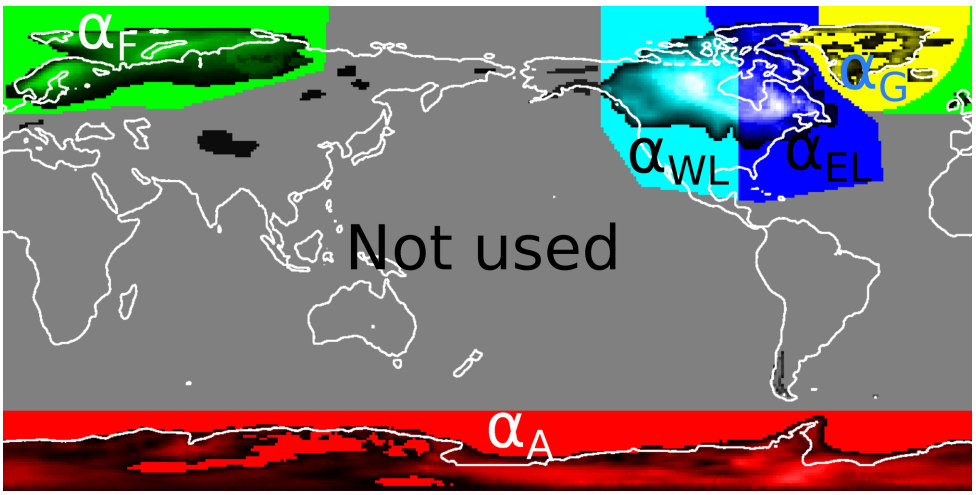

Figure 2. Map of the different ice regions considered in the inversion. Each region is indicated by a different hue, while ice in the grey region is neglected. For purposes of visual clarity the ice extension and ice thickness maxima, the temporal integration of the ANU model over the last 122 kyr is represented in shades of dark (note that the present-day ice thickness is subtracted because it does not participate to the GIA signal).

ice model, using a linear least square method (see Appendix A1.3). This method allows us to sample the parameter space and express the likelihood of each model:

$$p(\boldsymbol{y}|\boldsymbol{x}) = \exp\left(-\sum_{i=1}^{N_{\text{data}}} \frac{{w_i}^2}{2\sigma^2_{\text{dataset}}} \left(\frac{\boldsymbol{y}_i^m(\boldsymbol{x}) - \boldsymbol{y}_i^d}{\epsilon_i}\right)^2\right), \quad (1)$$

where $\boldsymbol{x}$ is the vector of parameters, $\boldsymbol{y}^d$ the constraining data set, $\boldsymbol{y}^m(\boldsymbol{x})$ the model predictions with parameters $\boldsymbol{x}$, $\boldsymbol{\epsilon}$ the uncertainty of the data, σ_{dataset} the standard deviation of the data set, $\boldsymbol{w}$ a vector of weights (see Appendix A2) accounting for the data distribution in space and time, which is meant to avoid over-fitting a single region or epoch with abundant data, and N_{data} the number of data.

With a sufficiently large sampling in the model space, this formulation allows a statistical characterization of each parameter x_i, yielding its:

(i) best fit $x_{i,\,\text{best}} = x_i(p = \max(p))$,
(ii) expected value $E(x_i) = \sum_{j=1}^{N_{\text{models}}} p_j x_{i,j}$,
(iii) standard deviation $\sigma(x_i) = \sum_{j=1}^{N_{\text{models}}} p_j (x_{i,j} - E(x_i))^2$,
(iv) Q per cent confidence interval $C_I = [l,\ u]$ such that $\sum_{x_i=l}^{x_i=u} p = Q.10^{-2}$,
(v) linear correlation coefficient to the other parameters $\rho(x_i, x_k) = \sum_{j=1}^{N_{\text{models}}} p_j \frac{(x_{i,j} - E(x_i))(x_{k,j} - E(x_k))}{\sigma(x_i)\sigma(x_k)}$.

Please note that upon occasion the correlation is nonlinear. In the general case, it is thus best illuminated by projecting the probability distribution over the 2-D space formed by the pair of parameters considered, rather than the linear correlation coefficient.

We use a uniform prior distribution within the explored parameter space, so that the *a posteriori* probability is equivalent to the likelihood. Note that in eq. (1) a normalizing constant could be added so that the integration of the probability would yield 1. However, while we do normalize it in our statistical calculations, in our probability plots we choose not to repeat this, so that we can still directly compare inversions with different ice models or rheologies: that way, we can affirm that a given probability value corresponds to the same misfit in all the inversions, and that models reaching a higher peak of probability perform better. Consequently, we advise the reader to compare the probability values of the different inversions rather than focusing on the meaning of their absolute values.

3 RESULTS

Our inversions are constrained by 5720 palaeo sea level records, dating up to 35 kyr BP, compiling near field records in Laurentia from Dyke & Peltier (2000), in Fennoscandia from Lambeck *et al.* (2010) and far-field records from Lambeck *et al.* (2014). We use ice-sheet histories either based on the ANU model (Lambeck *et al.* 2014) or on the ICE-5G model (Peltier 2004) and both Maxwell and Burgers rheologies. The inversions presented in this section use eight free parameters, of which three are resolved via the Bayesian method, and each inversion contains about 3×10^4 forward models. Inversion results are presented in additional detail in Appendix A3, along with Burgers inversions where the shear modulus and viscosity long-term to short-term ratio are added to the list of free parameters, instead of being fixed to a value of 5. In these cases, the number of models in each inversion reaches about 10^5.

3.1 ANU

Fig. 3(a) represents the *a posteriori* probability distribution (both on the *y*-axis and colour bar) in the Maxwell case projected in the η_{LM} dimension. The dashed-line highlights the apparent distribution envelope. This isolates the maximum probability that can be reached for a given value of η_{LM}. In Figs 3(b)–(d), the Maxwell case *a posteriori* probability distribution (coloured points) is projected against η_{LM}, in the *x*-axis. Here the upper-mantle viscosity η_{UM}, ice coefficient for East Laurentide α_{EL} and ice coefficient for Antarctica α_A are on the *y*-axis. The black cross indicates where the best-fitting model is located. Note that models with higher probability are plotted on top of the lower probability models, so that the envelope of the distribution is apparent. One could argue that representing the integration of the probability with respect to the other parameters might have much statistical relevance, but we found that the shape of the distribution is better highlighted with the projection method. Indeed, one can track a particular model (e.g. the best-fitting model) with its colour, or follow the good-fitting region when varying one parameter. For this purpose, we plot the black dash-dot line that describes the line along which the probability decreases the least, indicating a partial compensation between the parameters with respect to the misfit, which can be called a trade-off or correlation effect. Note that maps that include at least one ice coefficient as

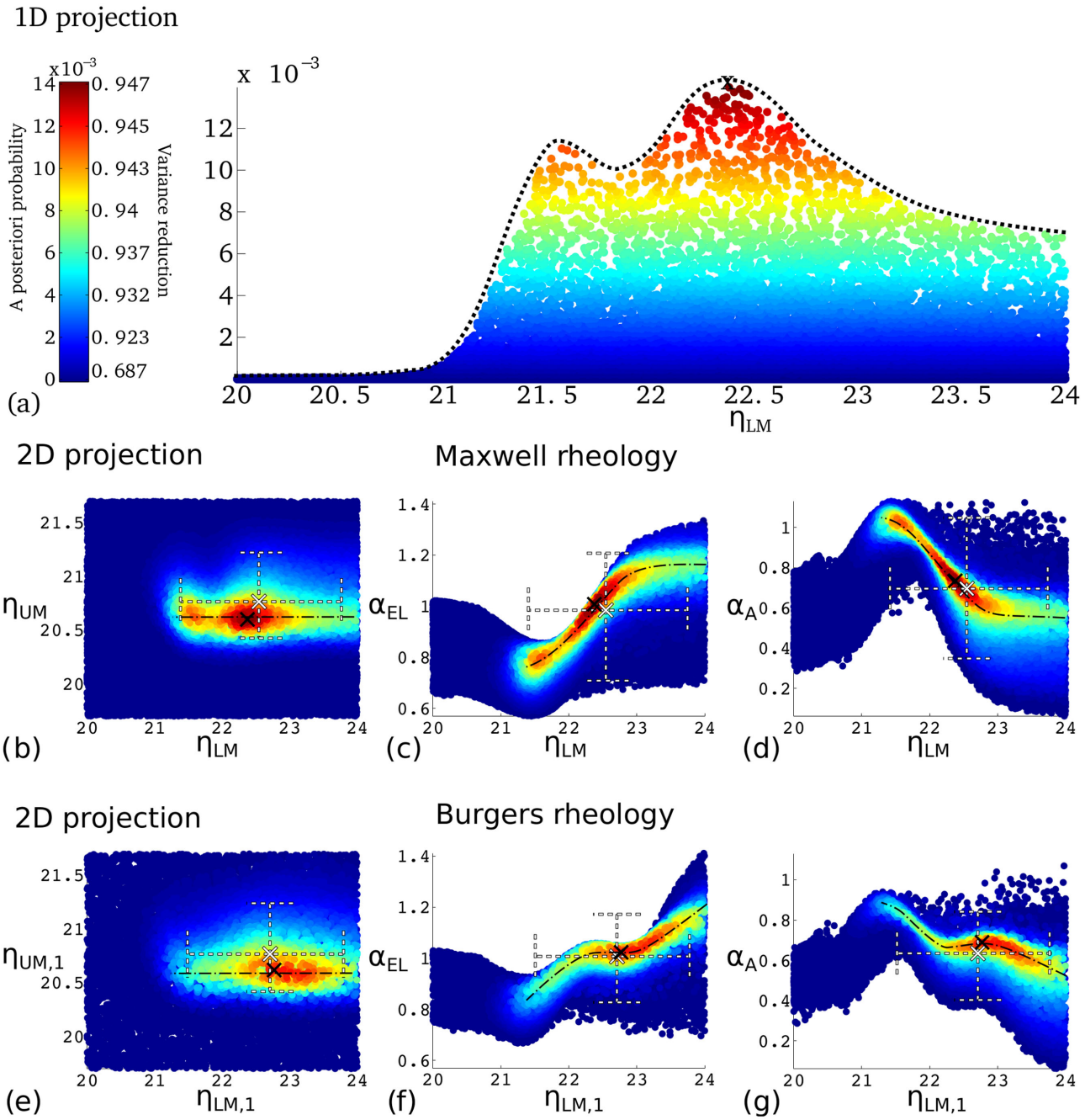

Figure 3. (a) Projected *a posteriori* probability in the Maxwell rheology case, as a function of the lower-mantle viscosity, with the ANU model as reference ice model. The dashed line highlights the distribution envelope, that is, max(p) for a given value of η_{LM}. (b–d) Maps of the envelope probability in the Maxwell rheology case. The dash-dot line is a visual guide that indicates the apparent trade-off axis, with the probability decreasing the least along this line. The black cross marks the position of the best-fitting model. The white cross indicates the expected model, and the dashed white line the 90 per cent confidence interval. (e–g) Maps of the envelope probability in the Burgers rheology case.

a parameter appear with some blank areas. This is perfectly expected as these coefficients are solved by least-squares methods, so the sampled area does not have a rectangular shape. These blank regions are, in fact, areas where the probability is very low. For a more complete description of the inverse results, see Appendix A3 where we display the probability distribution projected against each pair of parameters.

Similarly, Figs 3(e)–(g) represent the *a posteriori* probability distribution in the Burgers rheology case projected against $\eta_{\mathrm{LM},1}$ and, respectively, $\eta_{\mathrm{UM},1}$, α_{EL} and α_A. Note that the viscous parameters represented here correspond to the long-term value, while the transient viscosity can be recovered using the $10^{\eta_1}/10^{\eta_2}$ ratio. In this case, we fixed μ_1/μ_2 and $10^{\eta_1}/10^{\eta_2}$ to 5 so that we can illustrate the preferences , in the parameters space, that the solutions have when the Burgers contribution is sufficiently important. However, the reader should be advised that we could not constrain the values for these two parameters (see Figs A4 and A7 in Appendix A3). For purpose of comparison, the following values have been previously used in GIA and post-seismic modelling: $\mu_1/\mu_2 = 10$, $10^{\eta_1}/10^{\eta_2} = 10$ (Yuen *et al.* 1986), $\mu_1/\mu_2 = 1$, $10^{\eta_1}/10^{\eta_2} = 28$

Table 1. Contribution of the different ice regions when $\alpha = 1$ at the LGM. ξ is the equivalent eustatic sea level contribution, corresponding to the ratio of the ice volume to the oceanic surface area.

		WL	EL	F	A	G
ANU	ξ (m)	− 42.73	− 41.69	− 21.67	− 30.78	− 3.72
	Ice volume ($km^3 \times 10^6$)	15.10	14.74	7.66	10.88	1.31
ICE-5G	ξ (m)	− 54.97	− 30.87	− 23.45	− 18.58	− 2.51
	Ice volume ($km^3 \times 10^6$)	19.43	10.91	8.29	6.57	0.89

Table 2. Inversion results for the Maxwell case based on the ANU model as an ice model reference.

	Low η_{LM} maximum (P1)	High η_{LM} maximum (P2)	Expected value ± standard deviation	90 per cent confidence interval	
η_{UM}	20.628	20.599	20.764 ± 0.240	[20.428,	21.219]
η_{LM}	21.568	22.376	22.545 ± 0.722	[21.391,	23.762]
T_e	89.41	94.07	103.76 ± 28.90	[61.05,	156.19]
α_{WL}	0.729	0.882	0.918 ± 0.125	[0.728,	1.113]
α_{EL}	0.797	1.008	0.985 ± 0.160	[0.710,	1.206]
α_F	0.935	1.000	1.106 ± 0.216	[0.907,	1.575]
α_A	1.024	0.735	0.695 ± 0.214	[0.350,	1.046]
α_G	1.470	1.116	1.373 ± 0.511	[0.741,	2.416]
ξ_{LGM}	− 121.63	− 128.15	-130.76 ± 8.31	[−146.81,	−119.76]

Table 3. Inversion results for the Burgers rheology, with $\mu_1/\mu_2 = 5$ and $10^{\eta_1}/10^{\eta_2} = 5$, based on the ANU model as an ice reference. Note that $\eta_{UM,\,1}$ and $\eta_{LM,\,1}$ are the long-term viscosities.

	Low $\eta_{LM,\,1}$ maximum (P1)	High $\eta_{LM,\,1}$ maximum (P2)	Expected value ± standard deviation	90 per cent confidence interval	
$\eta_{UM,\,1}$	N/A	20.617	20.766 ± 0.250	[20.419,	21.236]
$\eta_{LM,\,1}$	N/A	22.771	22.708 ± 0.698	[21.493,	23.791]
T_e	N/A	92.29	97.74 ± 26.24	[55.76,	141.52]
α_{WL}	N/A	0.899	0.931 ± 0.073	[0.809,	1.062]
α_{EL}	N/A	1.023	1.007 ± 0.096	[0.828,	1.171]
α_F	N/A	1.089	1.213 ± 0.196	[1.037,	1.627]
α_A	N/A	0.690	0.635 ± 0.124	[0.405,	0.840]
α_G	N/A	1.419	1.705 ± 0.520	[1.094,	2.846]
ξ_{LGM}	N/A	− 131.17	-133.93 ± 5.95	[−145.71,	−126.03]

(Pollitz 2005), $\mu_1/\mu_2 = 3.3$, $10^{\eta_1}/10^{\eta_2} = 10$ (Spada *et al.* 2011b), $\mu_1/\mu_2 = 3$, $10^{\eta_1}/10^{\eta_2} = 10$ (Trubienko *et al.* 2013), $\mu_1/\mu_2 = 1$, $10^{\eta_1}/10^{\eta_2} > 7.5$ (Meade *et al.* 2013).

In Figs 3(a)–(d), two local maxima can be observed around $\eta_{LM} = 21.5$ (peak one, hereafter noted P1) and $\eta_{LM} = 22.4$ (P2), nevertheless we can see that a large set of models with $21.3 \leq \eta_{LM} \leq 24$ have a rather high probability, which we arbitrarily define here as more than two thirds of the maximum probability in order to describe the geometry of the probability distribution. This means that the uncertainty over η_{LM} is large and so the information gained over this parameter after the inversion is small. However, Figs 3(c) and (d) reveal that there is a significant gain of information over the correlation between η_{LM} and the ice distribution. Indeed, the region of good fit is clearly organized along a line that is neither horizontal or vertical, such that, in order to stay in the high probability region when increasing the lower-mantle viscosity from $10^{21.5}$ Pa s to $10^{22.4}$ Pa s (from P1 to P2), one has to increase the amount of ice in East Laurentide by about 20 per cent while decreasing the amount of ice that melted since the LGM in Antarctica by about 30 per cent. See Table 1 for conversion of the α values into eustatic sea level or ice volume equivalent. Let us note that for $\eta_{LM} \geq 23$ a plateau is reached along the trade-off line, which we interpret as a saturation effect of the lower-mantle viscous response. Table 2 summarizes the parameters of the two maxima and the statistics derived from the whole distribution for this inversion. Note that in addition to the standard deviation, we display the 90 per cent confidence interval which is more accurate to describe the uncertainty in the case of non-Gaussian distributions. Figs 3(e)–(g) reveal that adding a significant transient relaxation tends to increase the long-term lower-mantle viscosity by a small factor (approximately 1.5), with the best-fitting value being about $\eta_{LM,\,1} = 22.77$. Let us remark that P1 disappears in this case. Accordingly, the ice scenario is set to a higher ice volume in Laurentide and a lower ice volume in Antarctica, although the trade-off seems to be nonlinear with a plateau in the solutions with $22.3 \leq \eta_{LM,\,1} \leq 23$. Note that the value for $\eta_{UM,\,1}$ remains the same as for the Maxwell case. Table 3 details the parameter results in the Burgers ANU-based inversion.

3.2 ICE-5G

We performed a second set of inversions using ICE-5G as the reference ice model, which, while regionally adjusted in the same fashion as that for the ANU model, features differences in spatial and temporal ice distribution within each region. This allows us to understand the importance of such differences in the global fit and high probability region shape in the parameter space. Looking at the Fig. 4 colour bar, we immediately notice that the *a posteriori* probability drops by a factor of 10, corresponding to an RMS misfit in the sea level increasing from approximately 8–12 m. This is not surprising as we based our inversions on the data set used to establish the ANU model, and the reverse situation could be expected if

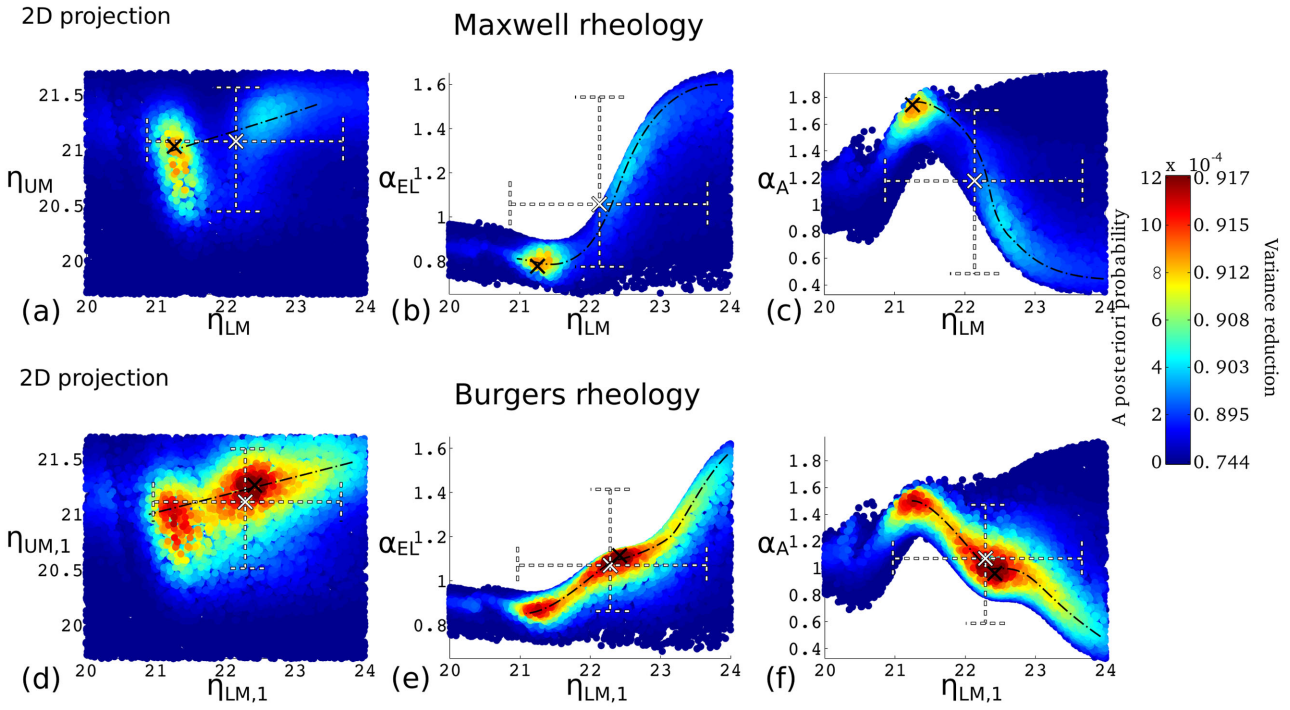

Figure 4. (a–c) Maps of the envelope probability in the Maxwell rheology case with the ICE-5G model as base reference for ice distribution. The dash-dot line is a visual guide that indicates the apparent trade-off axis, with the probability decreasing the least along this line. The black cross marks the position of the best-fitting model. The white cross indicates the expected model, and the dashed white line the 90 per cent confidence interval. (d–f) Maps of the envelope probability in the Burgers rheology case.

Table 4. Inversion results for the Maxwell rheology based on the ICE-5G model as an ice reference.

	Low $\eta_{\rm LM}$ maximum (P1)	High $\eta_{\rm LM}$ maximum (P2)	Expected value ±standard deviation	90 per cent confidence interval
$\eta_{\rm UM}$	21.034	21.285	21.070 ± 0.340	[20.442, 21.554]
$\eta_{\rm LM}$	21.257	22.542	22.138 ± 0.915	[20.864, 23.666]
T_e	16.42	110.96	96.68 ± 44.96	[26.45, 177.23]
$\alpha_{\rm WL}$	0.621	0.751	0.703 ± 0.073	[0.599, 0.834]
$\alpha_{\rm EL}$	0.778	1.239	1.056 ± 0.268	[0.775, 1.539]
α_F	0.745	1.222	1.046 ± 0.344	[0.728, 1.754]
α_A	1.744	0.856	1.179 ± 0.419	[0.492, 1.699]
α_G	2.015	2.975	2.497 ± 1.058	[0.859, 4.124]
$\xi_{\rm LGM}$	−113.04	−131.56	-124.08 ± 10.83	[−143.29, −111.24]

we were using the data set from which ICE-5G is derived. As in the ANU inversion, Fig. 4(a) reveals that there are two local maxima for the viscosity profile, one with a low viscosity increase between $\eta_{\rm UM} = 21$ (P1) and $\eta_{\rm LM} = 21.4$ and the other exhibiting a larger contrast with $\eta_{\rm UM} = 21.3$ and $\eta_{\rm LM} = 22.6$ (P2). We also note that, unlike the ANU case, the low viscosity solution is clearly preferred, and exhibits a larger uncertainty on $\eta_{\rm UM}$. Figs 4(b) and (c) show a trade-off effect very similar to the ANU case, although the percentage of ice change between the maxima is more important, reaching about 60 per cent more ice in Laurentide and 50 per cent less ice in Antarctica when moving from the P1 to the P2 solution. See Table 4 for all details on the Maxwell ICE-5G-based inversion results. Figs 4(d)–(f) display the results of the inversion for the Burgers rheology using $\mu_1/\mu_2 = 5$ and $10^{\eta_1}/10^{\eta_2} = 5$. The solutions feature a better maximum fit than in the Maxwell case, with the high and low viscosity solutions having about the same likelihood. The two maxima for the viscosities have the same location as in the Maxwell inversion, except for a small decrease of $\eta_{\rm LM,\,1}$ in the P2 maximum. The difference in ice coefficients is also smaller, with an increase of the ice mass by 30 per cent and a decrease of 50 per cent in Laurentide and Antarctica respectively, comparable to the results obtained in the ANU inversion. Table 5 summarizes the results in the Burgers ICE-5G-based inversion.

4 DISCUSSION

Possibilities for ice model improvement may reside in the distribution of the residuals. Indeed, Fig. 5 suggests that this distribution has common features for notably different rheology and α coefficient combinations. Perhaps imperfections in the ice model could be connected to these residuals that escape correction in our large-scale parameterization. Such conjecture suggests improvements to be discovered in either smaller scale features or in adjustments of time- dependence of the ice models.

Large residuals are found in all best solutions in the region of west Svalbard, Banks and Victoria Islands, between 9 and 15 kyr BP, so the models require significant small-scale improvement. It is worth

Table 5. Inversion results for the Burgers rheology, with $\mu_1/\mu_2 = 5$ and $10^{\eta_1}/10^{\eta_2} = 5$, based on the ICE-5G model as an ice reference. Note that $\eta_{\mathrm{UM},1}$ and $\eta_{\mathrm{LM},1}$ are the long-term viscosities.

	Low $\eta_{\mathrm{LM},1}$ maximum (P1)	High $\eta_{\mathrm{LM},1}$ maximum (P2)	Expected value $\pm$ standard deviation	90 per cent confidence interval
$\eta_{\mathrm{UM},1}$	20.973	21.263	21.113 ± 0.323	[20.514, 21.592]
$\eta_{\mathrm{LM},1}$	21.265	22.419	22.284 ± 0.852	[20.965, 23.658]
T_e	42.40	70.42	87.23 ± 43.39	[23.75, 166.92]
α_{WL}	0.694	0.780	0.762 ± 0.038	[0.698, 0.817]
α_{EL}	0.861	1.114	1.071 ± 0.168	[0.863, 1.415]
α_F	0.849	1.228	1.129 ± 0.255	[0.821, 1.603]
α_A	1.520	0.960	1.073 ± 0.272	[0.591, 1.472]
α_G	2.120	2.984	2.686 ± 0.900	[1.211, 4.100]
ξ_{LGM}	-118.15	-131.39	-128.07 ± 7.64	[-141.79, -117.38]

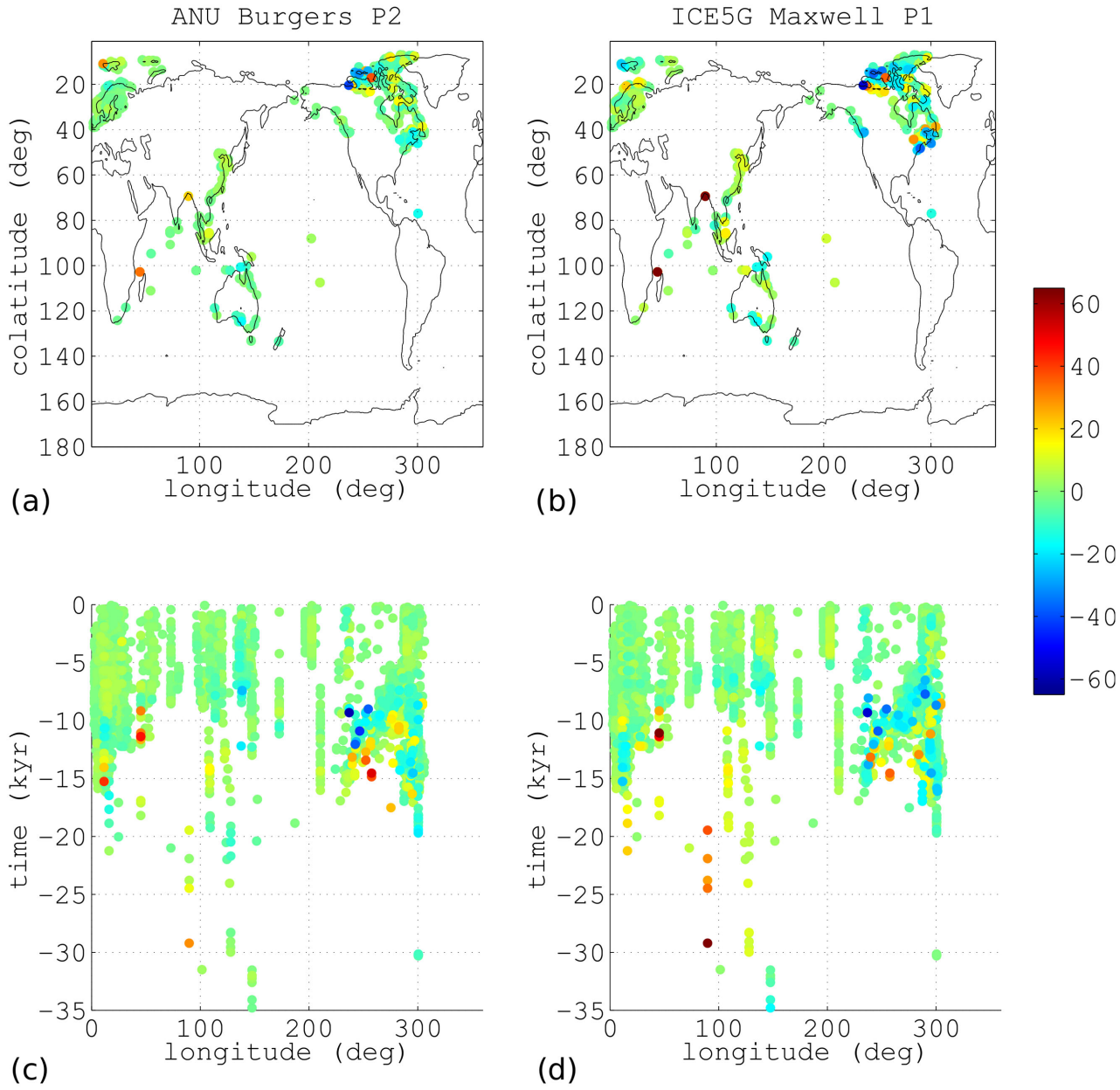

Figure 5. Weighted sea level residue distribution: $R_i = \frac{w_i(y_i^m - y_i^d)}{\epsilon_i}$, following Section 2.3 notations, for the following inversions: (a,c) P2 Burgers maximum with ANU-based ice model, (b,d) P1 Maxwell maximum with ICE-5G-based ice model. Note that points with higher absolute value are plotted on top of lower residue points, and that the scale is non-dimensional.

noting that the ice history of the Canadian Arctic Archipelago, in particular the Banks Island, has recently been significantly revised by Lakeman & England (2013). Larger scale residuals, with moderate to high amplitude, can be found over the Atlantic coast of North America prior to 6 kyr BP (particularly in the ICE-5G-based models), suggesting the potential for improvement in the Laurentian region ice history. We think that considering other ice history models in that region, such as Simon *et al.* (2015), could help to correct any biases that ANU and ICE-5G have in common, and could allow us to have better control over this region. In the far field, large local residuals can be observed in Mayotte and the Bengal fan regions, and are mainly due to very high precision data for their respective epoch. Here there are standard deviations that are less than 2 m, with data having substantial amplitude standout, between −120 and −135 m below the present-day level. At such locations the fit can be improved by a better timing of the global deglaciation, as these are mainly sensitive to the eustatic sea level. Note that both ANU-based and ICE-5G-based models show similar distributions of residuals, which is why Fig. 5 only displays the residuals of two models.

Our study demonstrates that GIA tends to bring different constraints on the parameters tested. The upper-mantle viscosity is the most sensitive parameter. The latter is bound between $10^{20.5}$ and 10^{21} Pa s in the ANU-based inversion, while in the ICE-5G-based inversion the upper range reaches $10^{21.5}$ Pa s. Our expected value is in agreement with the other global GIA and geodynamic inversions, for example, Lambeck (1990), Peltier (1994), Peltier (1996), Čadek & Fleitout (2003), Steinberger & Calderwood (2006) and Peltier & Drummond (2008), and, particularly in the ANU case seems to agree with estimates derived from decay times and relaxation spectra in the near-field (McConnell 1968; Parsons 1972; Mitrovica & Peltier 1993a,b; Mitrovica & Forte 2004; Martinec & Wolf 2005). In contrast, far-field data tend to prefer a value somewhat lower, between 10^{20} and $10^{20.3}$ Pa s citeplambeck2014, which highlights the fact that the viscosity profile in non-cratonic regions may be deviate from those derived from data located at the late-Pleistocene ice centres. Our global estimate is still biased towards the cratonic region profile rather than being a true lateral average of the mantle viscosity. This could be something integral to GIA inversion. First, the location of the ice sheets is mainly on or near cratons, and this local ice drives most of the GIA strain energy and deviatoric stress (Johnston *et al.* 1998) that occur in these regions. Second, the spatial distribution of our RSL data, tends to be relatively abundant around these regions. As additional data from the far field are included in the model, this situation could be considerably improved upon, for example, Bradley *et al.* (2016). The introduction of Burgers rheology influences mainly the large wavelength signal (Yuen & Peltier 1982), minimally controlled by the upper mantle, and therefore has little impact on the viscosity retrieved. The lithospheric thickness T_e seems to be independent of the other parameters, constrained to lie around a value of 95km with moderate uncertainty (see Appendix A), although in the ICE-5G inversion no minimum value can be retrieved.

On the other hand, the lower-mantle viscosity value is poorly constrained. Any value greater than 10^{21} Pa s can generate models with significant probability, provided that the ice model is correctly adjusted. Indeed, while the lower-mantle viscosity itself cannot be constrained, our analysis highlights very clear trade-off effects between the different coefficient for ice distribution and the lower-mantle viscosity. This trade-off is reflecting the coupled nature of the information contained in the RSL data. We still determine two local maxima for the lower-mantle viscosity, as classically acknowledged in GIA inversions since O'Connell (1971). For all inversions, the first one (P1) has a value lying in the $[10^{21.2}, 10^{21.7}]$ Pa s range, a value similar to Peltier (1994), Peltier (1996), Peltier & Drummond (2008) and Geruo *et al.* (2013) models, which have commonly been used as a reference to correct for the GIA signal in GRACE (Shepherd *et al.* 2012). The second maximum (P2) ranges between 10^{22} and 10^{23} Pa s, exhibiting a large viscosity contrast between upper mantle and lower mantle, consistent with inversions of geoid and seismic tomographic data (Hager & Richards 1989; Ricard & Wuming 1991; King & Masters 1992; Ricard *et al.* 1993; Čadek & Fleitout 1999, 2003; Steinberger & Calderwood 2006; Greff-Lefftz *et al.* 2016), inferences of viscosity from the sinking speed of subducted lithosphere (Čížková *et al.* 2012), analyses of deglaciation-induced changes in the dynamic flattening and rotation of the Earth (O'Connell 1971; Johnston & Lambeck 1999; Kaufmann & Lambeck 2002) and GIA calculations by Nakada & Lambeck (1988), Lambeck (1990), Wolf *et al.* (2006), Lambeck *et al.* (2014) and Nakada *et al.* (2015). P2 is also consistent with gradiometric GIA signal over the Laurentia region (Métivier *et al.* 2016), while P1 yields a signal one order of magnitude too small.

The viscosity profiles of Mitrovica & Forte (2004), obtained by a joint inversion of GIA and geoid related to mantle dynamics, are less straightforward in comparing to our results. While their average lower-mantle viscosity is large, comparable to P2, the authors do not emphasize a lower average of this viscosity, but rather the average viscosity between 660 and 1300 km. The bottom of this region is approximately the depth to which the sensitivity of GIA tails off with increasing depth in the lower mantle (Mitrovica 1996), and the average value in the region is closer to P1, hence manifesting signals that are also similar to our P1-generated GIA predictions. Here we have demonstrated the coupling of P1 and P2 solutions to ice loading variations, particularly when using the Burgers rheology. As a consequence our results are quite explicable in comparing to the geoid and GIA inversion results of Mitrovica & Forte (2004) as the latter employ a single ice load history. It would be interesting to advance models in the future that allow more freedom for ice history variation in the execution of joint inversions of mantle dynamics and GIA information.

When comparing the Burgers and Maxwell rheologies, we note that maximum probability values and confidence intervals are very similar, suggesting that neither of them exhibits superior performance in GIA inversions. However, note that in the Burgers case, either P1 is demoted (as in an ANU-based inversion) or P2 is promoted to a similar probability status to the case when P1 is preferred (as in an ICE-5G-based inversion). In either event, the likelihood of P2 (relative to P1) is enhanced by the assumption of the bi-viscous Burgers rheology. We find that this rheology is as likely as Maxwell rheology to reconcile the GIA signal. However, the physics to the former are consistent with the shallow mantle behaviour that ubiquitously explain post-seismic deformation and creep experiments. Consequently, the former is a serious competitor to Maxwell stress relaxing materials for developing GIA inversions. Some caution, however, is warranted, as we cannot reliably constrain any preference for the elastic components inherent to Burgers materials: μ_1/μ_2 and $10^{\eta_1}/10^{\eta_2}$, although we suggest values between 1 and 10 for both. Indeed, we note that a larger ratio substantially degrades the fit, while a ratio below 1 yield predictions that mimic those of Maxwell rheology so closely that they defeat the purpose of introducing a transient relaxation.

Compared to P1, P2 is associated with an increase of the ice volume by about 20 to 30 per cent in Laurentide (except for a more modest increase of the west Laurentide cap in the ICE-5G

case), an increase of 10 to 40 per cent in Fennoscandia. The latter are necessary to compensate the drop in signal amplitude due to the higher viscosity in the early deglaciation, and a decrease of some 40 per cent of the volume change in Antarctica. With relatively sparse RSL data in the near field of Antarctica, the model reduction counterbalances the increase of ice melt in the other ice sheets. It has been pointed out that the ICE-5G and ANU models overestimate the volume of ice on Antarctica (Nakada & Lambeck 1988; Nakada *et al.* 2000; Ivins & James 2005; Philippon *et al.* 2006; Pollard & DeConto 2009; Whitehouse *et al.* 2012; Ivins *et al.* 2013; Lambeck *et al.* 2014), which seems to be further supported by recent estimations of the ice retreat scenarios in West Antarctica around the LGM (Halberstadt *et al.* 2016). Hence, our inference of a reduction of Antarctic LGM volume appears to be an improvement in terms of ice volume distribution with respect to both the ICE-5G and ANU models (for extensive information of the state of the art on the Antarctic ice sheet reconstruction, see Briggs *et al.* 2013). A revised GIA prediction is especially important in the context of determining present-day mass balance from the GRACE signal. In the course of our study, Argus *et al.* (2014); Peltier *et al.* (2015) developed the ICE-6G model, essentially an update to ICE-5G, with reduced ice mass over Antarctica by ∼22 per cent. The reduction is a feature that we support with a P2-type model and that appears in both of the new models published by Whitehouse *et al.* (2012), Ivins *et al.* (2013) and Briggs *et al.* (2013). However, with a P1-type model, we would have to increase the ice mass of the Laurentide and/or Fennoscandia ice sheets in order to fit the far-field data, which in turns creates misfit in the near field of these regions. Our results do not seem to support both a low α_A and a P1-type model. Moreover, the authors of ICE-5G decreased the mass in West Laurentide relative to East Laurentide, which is a feature that we consistently find in our inversions, as illustrated in Appendix A3. The Greenland ice sheet appears to play the same role as the Antarctic ice sheet in regards to the fit of the far-field signal, as the surrounding sea level data are overwhelmed by the Laurentide signal. However, because of its modest contribution to the eustatic sea level it is affected by very large uncertainties. These results emphasize that there are both location- and time-related issues in the data sampling and these can influence the derived ice parameters, and this echoes a conclusion reached recently by Steffen *et al.* (2014). Finally, our data set is dominated by sea level records of ages ranging from 0 to 15 kyr BP, and a sparsely samples ages near the LGM. Hence, constraints are weaker over the LGM state. Our results show that while the local maxima models are able to have a very similar fit of the sea level data overall, the amplitude of the lowstand in sea level at the LGM decreases by as much as 15 m in contrasting P1-type and P2-type solutions, respectively.

While the ICE-5G and ANU-based inversions are similarly affected by the ice–mantle trade-offs and change in rheology, the parameters values and uncertainties retrieved in the inversions can be quite different, especially for the mantle viscosity, despite our scaling of the ice load on a regional level. This means that the regional distribution of the load, and even more probably the timing of the ice history, plays an important role in determining the GIA parameters. As such, the GIA inversions using RSL data suffer from a model-dependence. In particular, note that in ICE-5G-based inversions, P1 and P2 solutions result in differing upper-mantle viscosity, which, according to the results reported in Figs A5–A7, and this further exacerbates the ice–mantle trade-offs. We speculate that part of the discrepant upper-mantle viscosity values associated with ICE-5G and ANU models owe to differences in the timing of deglaciation events. We also infer that the timing difference between ICE-5G and ANU is a fundamental discriminating feature and underlies the differences in the two model performances with respect to our RSL data set. We see this by comparing the maximum probability obtained with either ice model. Note that since we use the same constraining data set as the ANU model, it was expected that ANU-based inversions were going to perform better. Had we been using the same constraining data set as ICE-5G, and assuming no major difference in the method or data treatment, we would have expected our ICE-5G-based inversions to be superior to the ANU-based inversions. While it is quite natural for us to have chosen the larger ANU RSL data set, significant progress could be achieved toward reducing the non-uniqueness of the GIA solutions if the respective models had considered precisely the same constraining RSL data sets. Our recommendation is to build a common, accessible and consistent RSL data set for the GIA community (Düsterhus *et al.* 2016).

Many of the previous inversions involving GIA or mantle rheology have focused on presenting a limited number of their best-fitting models, even when testing a large set of models, (Lambeck 1990; Ricard *et al.* 1993; Peltier 1994, 1996; Steinberger & Calderwood 2006; Peltier & Drummond 2008), and have thus been illustrating only a limited part of the parameter space. In contrast here we emphasize the importance of exploring a broader set of parameters for GIA inversions, and in particular exploring a joint parameter space of ice history and rheology. To this end, we advocate the use of Bayesian methods, much like Mitrovica & Peltier (1991), Mitrovica & Peltier (1993a,b, 1995); Mitrovica (1996), Cianetti *et al.* (2002), Martinec & Wolf (2005) and Lambeck *et al.* (2014), and the use of the full probability density function as much as the graphical representation of a high-dimensional object allows it. Not only does it reveal the best model, but also the existence of multiple maxima and trade-off effects, and provides a way to estimate the uncertainty of the parameters inverted, and similarly for the model predictions (e.g. ξ_{LGM}, see Tables 2–5).

5 CONCLUSIONS

We have explored the parameter space of GIA models by a Bayesian method, investigating the mantle rheology and the ice history, thus clarifying a non-uniqueness in the GIA solutions and highlighting the range of uncertainty and illuminating trade-offs that should be better appreciated when evaluating the parameter solutions retrieved in from inversion. Using 5720 palaeo sea level records as constraints, we are able to determine the upper-mantle viscosity to a value of $10^{20.77 \pm 0.25}$ Pa s ($10^{21.09 \pm 0.33}$ Pa s, for ICE-5G) and the lithospheric thickness to 100.75 ± 27.57 km (92.91 ± 43.67 km, for ICE-5G) using a scaled version of the ANU ice history model, as these parameters appear to be retrieved free of dependence on the other parameters. On the contrary, it seems impossible to determine the value of the lower-mantle viscosity, as any value larger than 10^{21} Pa s may provide a reasonable fit to the data set. We however determine strong trade-off effects between the lower-mantle viscosity and ice history, highlighting the need to invert jointly for ice history and mantle rheology in GIA when dealing with palaeo sea level records. The inversions typically yield two peaks with similar probability values: peak one (P1) features a low viscosity in the lower mantle between $10^{21.2}$ and $10^{21.7}$ Pa s, while peak two (P2) is characterized by a larger ice volume in Fennoscandia and Laurentia and a smaller volume in Antarctica than P1 and exhibits a larger viscosity between 10^{22} and 10^{23} Pa s. The latter is in agreement with most geodynamic inversions of the mantle viscosity and gravity

gradient anomalies over Laurentia. We have tested both Maxwell and Burgers rheologies and found that while the latter does not provide a better fit, nor a significantly different confidence interval of the parameters, it provides new insights regarding the P1/P2 ambiguity in GIA solutions by increasing the relative likelihood of a P2-type solution. It is also worth noting that transient relaxation as featured by the Burgers rheology opens up new interpretations of the mantle viscosity that are consistent with laboratory creep experiments and might especially be helpful in reconciling GIA with different time-scale phenomena, such as mantle convection. It should be noted, however, that we are not able to determine a best value for Burgers parameters. These features exist whether we choose the ANU or ICE-5G model as reference for our ice models, yet we find that they exhibit very different absolute maximum probability, relative probability of P2 to P1, and uncertainties. The emphasis in the present study on the peak P2, which has a large lower-mantle viscosity, may affect significantly many signals due to GIA not discussed here, such as geoid and gravity anomalies, horizontal velocities, etc. It may in turn affect corrections to GRACE gravity observations linked to GIA over Antarctica and the shallow seas that surround all formerly glaciated regions. We have emphasized the breadth of the solutions throughout the parameter spaces, and recommend that this be considered in future GIA inversions. Indeed, our Bayesian method allows for the calculation of uncertainties affecting GIA parameters and predictions, and thus provides a critical perspective on current and future GIA models.

ACKNOWLEDGEMENTS

We wish to thank Kurt Lambeck and Erik Ivins, who provided some very insightful discussions about the sea level data and ice history models. We also thank Pippa Whitehouse and Jerry Mitrovica for their very constructive review of the paper.

The computations involving spherical harmonics have been performed by means of program SHTOOLS (Wieczorek *et al.* 2016). This work is supported by the CNES (Centre National d'Études Spatiales) through the TOSCA committee and constitutes IPGP contribution no. 3827.

REFERENCES

Alterman, Z., Jarosch, H. & Pekeris, C., 1959. Oscillations of the earth, *Proc. R. Soc. A,* **252,** 80–95.

Amante, C. & Eakins, B.W., 2009. *ETOPO1 1 Arc-minute Global Relief Model: Procedures, Data Sources and Analysis,* US Department of Commerce, National Oceanic and Atmospheric Administration, National Environmental Satellite, Data, and Information Service, National Geophysical Data Center, Marine Geology and Geophysics Division Colorado.

Anderson, D.L. & Minster, J.B., 1979. The frequency dependence of q in the earth and implications for mantle rheology and chandler wobble, *Geophys. J. Int.,* **58**(2), 431–440.

Argus, D.F., Peltier, W., Drummond, R. & Moore, A.W., 2014. The Antarctica component of postglacial rebound model ICE-6G_C (VM5a) based on GPS positioning, exposure age dating of ice thicknesses, and relative sea level histories, *Geophys. J. Int.,* **198**(1), 537–563.

Beghin, P., Charbit, S., Dumas, C., Kageyama, M., Roche, D. & Ritz, C., 2014. Interdependence of the growth of the northern hemisphere ice sheets during the last glaciation: the role of atmospheric circulation, *Clim. Past,* **10**(1), 345–358.

Biot, M.A., 1962. Mechanics of deformation and acoustic propagation in porous media, *J. Appl. Phys.,* **33**(4), 1482–1498.

Bradley, S.L., Milne, G.A., Horton, B.P. & Zong, Y., 2016. Modelling sea level data from China and Malay-Thailand to estimate Holocene ice-volume equivalent sea level change, *Quat. Sci. Rev.,* **137,** 54–68.

Briggs, R., Pollard, D. & Tarasov, L., 2013. A glacial systems model configured for large ensemble analysis of Antarctic deglaciation, *Cryosphere,* **7**(6), 1949–1970.

Čadek, O. & Fleitout, L., 1999. A global geoid model with imposed plate velocities and partial layering, *J. geophys. Res.,* **104**(B12), 29 055–29 075.

Čadek, O. & Fleitout, L., 2003. Effect of lateral viscosity variations in the top 300 km on the geoid and dynamic topography, *Geophys. J. Int.,* **152**(3), 566–580.

Chambers, D.P. & Bonin, J., 2012. Evaluation of release-05 grace time-variable gravity coefficients over the ocean, *Ocean Sci.,* **8**(5), 859–868.

Charbit, S., Ritz, C., Philippon, G., Peyaud, V. & Kageyama, M., 2007. Numerical reconstructions of the northern hemisphere ice sheets through the last glacial-interglacial cycle, *Clim. Past,* **3**(1), 15–37.

Church, J.A. *et al.*, 2013. Sea level change, in *Climate Change 2013: The Physical Science Basis. Contribution of Working Group I to the Fifth Assessment Report of the Intergovernmental Panel on Climate Change,* pp. 1137–1216, eds Stocker, T.F. *et al.*, Cambridge Univ. Press.

Cianetti, S., Giunchi, C. & Spada, G., 2002. Mantle viscosity beneath the Hudson bay: an inversion based on the Metropolis algorithm, *J. geophys. Res.,* **107**(B12), ETG 12-1–ETG 12-15.

Čížková, H., van den Berg, A.P., Spakman, W. & Matyska, C., 2012. The viscosity of Earths lower mantle inferred from sinking speed of subducted lithosphere, *Phys. Earth planet. Inter.,* **200,** 56–62.

Clark, C.D., Evans, D.J., Khatwa, A., Bradwell, T., Jordan, C.J., Marsh, S.H., Mitchell, W.A. & Bateman, M.D., 2004. Map and GIS database of glacial landforms and features related to the last British Ice Sheet, *Boreas,* **33**(4), 359–375.

Craig, T., Calais, E., Fleitout, L., Bollinger, L. & Scotti, O., 2016. Evidence for the release of long-term tectonic strain stored in continental interiors through intraplate earthquakes, *Geophys. Res. Lett.,* **43**(13), 6826–6836.

Düsterhus, A. *et al.*, 2016. Palaeo sea-level and ice-sheet databases: problems, strategies and perspectives, *Clim. Past,* **12**(4), 911–921.

Dyke, A.S. & Peltier, W., 2000. Forms, response times and variability of relative sea-level curves, glaciated North America, *Geomorphology,* **32**(3), 315–333.

Dyke, A.S. & Prest, V.K., 1987. Late Wisconsinan and Holocene history of the Laurentide ice sheet, *Géogr. Phys. Quat.,* **41**(2), 237–263.

Dziewonski, A.M. & Anderson, D.L., 1981. Preliminary reference earth model, *Phys. Earth planet. Inter.,* **25**(4), 297–356.

Farrell, W., 1972. Deformation of the Earth by surface loads, *Rev. Geophys.,* **10**(3), 761–797.

Farrell, W. & Clark, J.A., 1976. On postglacial sea level, *Geophys. J Int.,* **46**(3), 647–667.

Fleitout, L., Krien, Y. & Cailletaud, G., 2006. Post-glacial rebound: lateral viscosity variations, transient creep and the constraints on Holocene ice-sheets, *Geophys. Res. Abstr.,* **8,** 09224.

Forte, A.M. & Mitrovica, J.X., 1996. New inferences of mantle viscosity from joint inversion of long-wavelength mantle convection and post-glacial rebound data, *Geophys. Res. Lett.,* **23**(10), 1147–1150.

Forte, A.M. & Peltier, R., 1991. Viscous flow models of global geophysical observables: 1. Forward problems, *J. geophys. Res.,* **96**(B12), 20 131–20 159.

Geruo, A., Wahr, J. & Zhong, S., 2013. Computations of the viscoelastic response of a 3-D compressible Earth to surface loading: an application to Glacial Isostatic Adjustment in Antarctica and Canada, *Geophys. J Int.,* **192**(2), 557–572.

Greff-Lefftz, M. & Legros, H., 1997. Some remarks about the degree-one deformation of the earth, *Geophys. J Int.,* **131**(3), 699–723.

Greff-Lefftz, M., Métivier, L., Panet, I., Caron, L. & Pajot-Métivier, G., 2016. Joint analysis of GOCE gravity gradients data with seismological and geodynamic observations to infer mantle properties, *Geophys. J. Int.,* **205,** 257–283.

Hager, B. & Richards, M., 1989. Long-wavelength variations in Earth's geoid: physical models and dynamical implications, *Phil. Trans. R. Soc. A,* **328**(1599), 309–327.

Hager, B.H., Clayton, R.W., Richards, M.A., Comer, R.P. & Dziewonski, A.M., 1984. Lower mantle heterogeneity, dynamic topography and the geoid, *Nature,* **313,** 541–545.

Halberstadt, A. R.W., Simkins, L.M., Greenwood, S.L. & Anderson, J.B., 2016. Past ice-sheet behaviour: retreat scenarios and changing controls in the ross sea, Antarctica, *Cryosphere,* **10**(3), 1003–1020.

Han, D. & Wahr, J., 1989. Post-glacial rebound analysis for a rotating earth, *Slow Deformation and Transmission of Stress in the Earth,* pp. 1–6, eds Cohen, S.C. & Vaníček, P., American Geophysical Union.

Han, S.-C., Sauber, J., Luthcke, S.B., Ji, C. & Pollitz, F.F., 2008. Implications of postseismic gravity change following the great 2004 Sumatra-Andaman earthquake from the regional harmonic analysis of grace intersatellite tracking data, *J. geophys. Res.,* **113,** B11413, doi:10.1029/2008JB005705.

Ivins, E., Sammis, C. & Yoder, C., 1993. Deep mantle viscous structure with prior estimate and satellite constraint, *J. geophys. Res.,* **98**(B3), 4579–4609.

Ivins, E.R. & James, T.S., 2005. Antarctic glacial isostatic adjustment: a new assessment, *Antarctic Sci.,* **17**(04), 541–553.

Ivins, E.R. & Sammis, C.G., 1996. Transient creep of a composite lower crust: 1. Constitutive theory, *J. geophys. Res.,* **101**(B12), 27 981–28 004.

Ivins, E.R., James, T.S., Wahr, J., Schrama, O., Ernst, J., Landerer, F.W. & Simon, K.M., 2013. Antarctic contribution to sea level rise observed by grace with improved GIA correction, *J. geophys. Res.,* **118**(6), 3126–3141.

Ji, S. & Zhao, P., 1993. Flow laws of multiphase rocks calculated from experimental data on the constituent phases, *Earth planet. Sci. Lett.,* **117**(1), 181–187.

Ji, S. & Zhao, P., 1994. Strength of two-phase rocks: a model based on fiber-loading theory, *J. Struct. Geol.,* **16**(2), 253–262.

Johnston, P., 1993. The effect of spatially non-uniform water loads on prediction of sea-level change, *Geophys. J. Int.,* **114**(3), 615–634.

Johnston, P. & Lambeck, K., 1999. Postglacial rebound and sea level contributions to changes in the geoid and the Earth's rotation axis, *Geophys. J. Int.,* **136**(3), 537–558.

Johnston, P., Wu, P. & Lambeck, K., 1998. Dependence of horizontal stress magnitude on load dimension in glacial rebound models, *Geophys. J. Int.,* **132**(1), 41–60.

Kaufmann, G. & Lambeck, K., 2002. Glacial isostatic adjustment and the radial viscosity profile from inverse modeling, *J. geophys. Res.,* **107**(B11), ETG 5-1–ETG 5-15.

King, S.D. & Masters, G., 1992. An inversion for radial viscosity structure using seismic tomography, *Geophys. Res. Lett.,* **19**(15), 1551–1554.

Kirkpatrick, S., Gelatt, C.D. & Vecchi, M.P., 1983. Optimization by simulated annealing, *Science,* **220**(4598), 671–680.

Lakeman, T.R. & England, J.H., 2013. Late Wisconsinan glaciation and postglacial relative sea-level change on western Banks Island, Canadian Arctic Archipelago, *Quat. Res.,* **80**(1), 99–112.

Lambeck, K., 1990. Glacial rebound sea-level change and mantle viscosity, *Q. J. R. Astron. Soc.,* **31,** 1–30.

Lambeck, K. & Nakada, M., 1990. Late Pleistocene and Holocene sea-level change along the Australian coast, *Palaeogeogr. Palaeoclimatol. Palaeoecol.,* **89**(1-2), 143–176.

Lambeck, K., Purcell, A., Johnston, P., Nakada, M. & Yokoyama, Y., 2003. Water-load definition in the glacio-hydro-isostatic sea-level equation, *Quat. Sci. Rev.,* **22**(2), 309–318.

Lambeck, K., Purcell, A., Zhao, J. & Svenson, N.-O., 2010. The Scandinavian ice sheet: from MIS 4 to the end of the Last Glacial Maximum, *Boreas,* **39**(2), 410–435.

Lambeck, K., Rouby, H., Purcell, A., Sun, Y. & Sambridge, M., 2014. Sea level and global ice volumes from the last glacial maximum to the Holocene, *Proc. Natl. Acad. Sci. USA,* **111**(43), 15 296–15 303.

Longman, I., 1962a. A Green's function for determining the deformation of the Earth under surface mass loads: 1. Theory, *J. geophys. Res.,* **67**(2), 845–850.

Longman, I., 1962b. A Green's function for determining the deformation of the Earth under surface mass loads: 2. Computations and numerical results, *J. geophys. Res.,* **68**(2), 485–496.

Love, A., 1909. The yielding of the Earth to disturbing forces, *Proc. R. Soc. A,* **82**(551), 73–88.

Marquardt, H. & Miyagi, L., 2015. Slab stagnation in the shallow lower mantle linked to an increase in mantle viscosity, *Nat. Geosci.,* **8**(4), 311–314.

Martinec, Z. & Wolf, D., 2005. Inverting the Fennoscandian relaxation-time spectrum in terms of an axisymmetric viscosity distribution with a lithospheric root, *J. Geodyn.,* **39**(2), 143–163.

McConnell, R.K., 1968. Viscosity of the mantle from relaxation time spectra of isostatic adjustment, *J. geophys. Res.,* **73**(22), 7089–7105.

Meade, B.J., Klinger, Y. & Hetland, E.A., 2013. Inference of multiple earthquake-cycle relaxation timescales from irregular geodetic sampling of interseismic deformation, *Bull. seism. Soc. Am.,* **103**(5), 2824–2835.

Melini, D., Cannelli, V., Piersanti, A. & Spada, G., 2008. Post-seismic rebound of a spherical Earth: new insights from the application of the Post-Widder inversion formula, *Geophys. J. Int.,* **174**(2), 672–695.

Métivier, L., Caron, L., Greff Lefftz, M., Pajot-Métivier, G., Fleitout, L. & Rouby, H., 2016. Evidence for postglacial signature in gravity gradients: a clue on lower mantle viscosity, *Earth planet. Sci. Lett.,* **452,** 146–156.

Metropolis, N. & Ulam, S., 1949. The Monte Carlo method, *J. Am. Stat. Assoc.,* **44**(247), 335–341.

Metropolis, N., Rosenbluth, A.W., Rosenbluth, M.N., Teller, A.H. & Teller, E., 1953. Equation of state calculations by fast computing machines, *J. Chem. Phys.,* **21**(6), 1087–1092.

Milne, G.A. & Mitrovica, J.X., 1998. Postglacial sea-level change on a rotating earth, *Geophys. J. Int.,* **133**(1), 1–19.

Mitrovica, J.X., 1996. Haskell [1935] revisited, *J. geophys. Res.,* **101**(B1), 555–569.

Mitrovica, J. & Forte, A., 2004. A new inference of mantle viscosity based upon joint inversion of convection and glacial isostatic adjustment data, *Earth planet. Sci. Lett.,* **225**(1), 177–189.

Mitrovica, J. & Peltier, W., 1991. A complete formalism for the inversion of post-glacial rebound data: resolving power analysis, *Geophys. J. Int.,* **104**(2), 267–288.

Mitrovica, J. & Peltier, W., 1993a. The inference of mantle viscosity from an inversion of the Fennoscandian relaxation spectrum, *Geophys. J. Int.,* **114**(1), 45–62.

Mitrovica, J. & Peltier, W., 1993b. A new formalism for inferring mantle viscosity based on estimates of post glacial decay times: application to RSL variations in N.E. Hudson bay, *Geophys. Res. Lett.,* **20**(20), 2183–2186.

Mitrovica, J. & Peltier, W., 1995. Constraints on mantle viscosity based upon the inversion of post-glacial uplift data from the Hudson bay region, *Geophys. J. Int.,* **122**(2), 353–377.

Mitrovica, J.X. & Forte, A.M., 1997. Radial profile of mantle viscosity: results from the joint inversion of convection and postglacial rebound observables, *J. geophys. Res.,* **102**(B2), 2751–2769.

Mitrovica, J.X., Milne, G.A. & Davis, J.L., 2001. Glacial isostatic adjustment on a rotating earth, *Geophys. J. Int.,* **147**(3), 562–578.

Munk, W.H. & MacDonald, G.J., 1960. *The Rotation of the Earth; A Geophysical Discussion,* Cambridge Univ. Press.

Nakada, M. & Lambeck, K., 1988. The melting history of the late Pleistocene Antarctic ice sheet, *Nature,* **333**(6168), 36–40.

Nakada, M., Kimura, R., Okuno, J., Moriwaki, K., Miura, H. & Maemoku, H., 2000. Late Pleistocene and Holocene melting history of the Antarctic ice sheet derived from sea-level variations, *Mar. Geol.,* **167**(1), 85–103.

Nakada, M., Okuno, J., Lambeck, K. & Purcell, A., 2015. Viscosity structure of earth's mantle inferred from rotational variations due to GIA process and recent melting events, *Geophys. J. Int.,* **202**(2), 976–992.

O'Connell, R.J., 1971. Pleistocene glaciation and the viscosity of the lower mantle, *Geophys. J Int.,* **23**(3), 299–327.

Panet, I., Pollitz, F., Mikhailov, V., Diament, M., Banerjee, P. & Grijalva, K., 2010. Upper mantle rheology from GRACE and GPS postseismic deformation after the 2004 Sumatra-Andaman earthquake, *Geochem. Geophys. Geosyst.,* **11,** Q06008, doi:10.1029/2009GC002905.

Parsons, B., 1972. Changes in the Earth's shape, *PhD thesis,* Department of Geodesy and Geophysics, Cambridge University, Cambridge.
Paulson, A., Zhong, S. & Wahr, J., 2007. Inference of mantle viscosity from grace and relative sea level data, *Geophys. J. Int.,* **171**(2), 497–508.
Peltier, W., 1974. The impulse response of a Maxwell Earth, *Rev. Geophys. Space Phys.,* **12**(4), 649–669.
Peltier, W.R., 1994. Ice age paleotopography, *Science,* **265,** 195–195.
Peltier, W.R., 1996. Mantle viscosity and ice-age ice sheet topography, *Science,* **273,** 1359–1364.
Peltier, W., 2004. Global glacial isostasy and the surface of the ice-age Earth: the ICE-5G (VM2) model and GRACE, *Annu. Rev. Earth Planet. Sci.,* **32,** 111–149.
Peltier, W.R. & Drummond, R., 2008. Rheological stratification of the lithosphere: A direct inference based upon the geodetically observed pattern of the glacial isostatic adjustment of the North American continent, *Geophys. Res. Lett.,* **35,** L16314, doi:10.1029/2008GL034586.
Peltier, W., Yuen, D. & Wu, P., 1980. Postglacial rebound and transient rheology, *Geophys. Res. Lett.,* **7**(10), 733–736.
Peltier, W., Argus, D. & Drummond, R., 2015. Space geodesy constrains ice age terminal deglaciation: The global ICE-6G_C (VM5a) model, *J. geophys. Res.,* **120**(1), 450–487.
Philippon, G., Ramstein, G., Charbit, S., Kageyama, M., Ritz, C. & Dumas, C., 2006. Evolution of the Antarctic ice sheet throughout the last deglaciation: a study with a new coupled climate—north and south hemisphere ice sheet model, *Earth planet. Sci. Lett.,* **248**(3), 750–758.
Pollard, D. & DeConto, R.M., 2009. Modelling West Antarctic ice sheet growth and collapse through the past five million years, *Nature,* **458**(7236), 329–332.
Pollitz, F.F., 2005. Transient rheology of the upper mantle beneath central Alaska inferred from the crustal velocity field following the 2002 Denali earthquake, *J. geophys. Res.,* **110,** B08407, doi:10.1029/2005JB003672.
Ricard, Y. & Wuming, B., 1991. Inferring the viscosity and the 3-D density structure of the mantle from geoid, topography and plate velocities, *Geophys. J. Int.,* **105**(3), 561–571.
Ricard, Y., Richards, M., Lithgow-Bertelloni, C. & Le Stunff, Y., 1993. A geodynamic model of mantle density heterogeneity, *J. geophys. Res.,* **98**(B12), 21 895–21 909.
Shepherd, A. *et al.*, 2012. A reconciled estimate of ice-sheet mass balance, *Science,* **338**(6111), 1183–1189.
Simon, K., James, T. & Dyke, A., 2015. A new glacial isostatic adjustment model of the Innuitian Ice Sheet, Arctic Canada, *Quat. Sci. Rev.,* **119,** 11–21.
Spada, G. *et al.*, 2011a. A benchmark study for glacial isostatic adjustment codes, *Geophys. J Int.,* **185**(1), 106–132.
Spada, G., Colleoni, F. & Ruggieri, G., 2011b. Shallow upper mantle rheology and secular ice sheet fluctuations, *Tectonophysics,* **511**(3), 89–98.
Steffen, H., Wu, P. & Wang, H., 2014. Optimal locations of sea-level indicators in glacial isostatic adjustment investigations, *Solid Earth,* **5**(1), 511–521.
Steinberger, B. & Calderwood, A.R., 2006. Models of large-scale viscous flow in the Earth's mantle with constraints from mineral physics and surface observations, *Geophys. J Int.,* **167**(3), 1461–1481.
Svendsen, J.I. *et al.*, 2004. Late quaternary ice sheet history of northern Eurasia, *Quat. Sci. Rev.,* **23**(11), 1229–1271.
Trubienko, O., Fleitout, L., Garaud, J.-D. & Vigny, C., 2013. Interpretation of interseismic deformations and the seismic cycle associated with large subduction earthquakes, *Tectonophysics,* **589,** 126–141.
Tushingham, A.M. & Peltier, W., 1992. Validation of the ICE-3G model of würm-wisconsin deglaciation using a global data base of relative sea level histories, *J. geophys. Res.,* **97**(B3), 3285–3304.
Watkins, M.M., Wiese, D.N., Yuan, D.-N., Boening, C. & Landerer, F.W., 2015. Improved methods for observing earth's time variable mass distribution with grace using spherical cap mascons, *J. geophys. Res.,* **120**(4), 2648–2671.
Whitehouse, P.L., Bentley, M.J., Milne, G.A., King, M.A. & Thomas, I.D., 2012. A new glacial isostatic adjustment model for Antarctica: calibrated and tested using observations of relative sea-level change and present-day uplift rates, *Geophys. J Int.,* **190**(3), 1464–1482.
Wieczorek, M.A., Meschede, M., Oshchepkov, I., de Andrade, E.S. & heroxbd 2016. SHTOOLS: Version 4.0, Zenodo, doi:10.5281/zenodo.206114.
Wolf, D., Klemann, V., Wünsch, J. & Zhang, F.-P., 2006. A reanalysis and reinterpretation of geodetic and geological evidence of glacial-isostatic adjustment in the Churchill region, Hudson Bay, *Surv. Geophys.,* **27**(1), 19–61.
Yuen, D.A. & Peltier, W., 1982. Normal modes of the viscoelastic earth, *Geophys. J Int.,* **69**(2), 495–526.
Yuen, D.A., Sabadini, R.C., Gasperini, P. & Boschi, E., 1986. On transient rheology and glacial isostasy, *J. geophys. Res.,* **91**(B11), 11 420–11 438.
Zweck, C. & Huybrechts, P., 2005. Modeling of the northern hemisphere ice sheets during the last glacial cycle and glaciological sensitivity, *J. geophys. Res.,* **110,** D07103, doi:10.1029/2004JD005489.

APPENDIX A: PRECISIONS ON THE METHOD AND FULL REPRESENTATION OF THE PROBABILITY DISTRIBUTIONS

A1 Theory

A1.1 Rheology

The usual rheology used in GIA inversion is the linearly relaxing viscoelastic Maxwell model. It features an instantaneous elastic response followed by a viscous creep similar to a Newtonian fluid, and is represented in analogous mechanical diagram by the association of a spring with Lamé coefficients λ_1 and μ_1, and a dashpot with viscosity η_1 in series. Following the correspondence principle (Biot 1962), it is possible to write the stress to strain relation in a form similar to Hooke's law:

$$\sigma(\omega) = \lambda(\omega)\nabla.\epsilon(\omega) + 2\mu(\omega)\epsilon(\omega). \tag{A1}$$

with ω the frequency, and using:

$$\mu(\omega) = \frac{\mu_1 i\omega}{i\omega + \frac{\mu_1}{\eta_1}}. \tag{A2}$$

$$\lambda(\omega) = \frac{\lambda_1 i\omega + \kappa\frac{\mu_1}{\eta_1}}{i\omega + \frac{\mu_1}{\eta_1}}. \tag{A3}$$

where $\kappa = \lambda_1 + \frac{2}{3}\mu_1$ and $\kappa = \lambda(\omega) + \frac{2}{3}\mu(\omega)$ is the bulk modulus, independent of the frequency.

Burgers rheology is a model that exhibits the same features as Maxwell rheology with an additional transient relaxation. It is described by a Kelvin–Voigt body, that is, a dashpot element with viscosity η_2 in parallel with a spring element with shear modulus μ_2, in series with a Maxwell body. Similarly, using the correspondence principle, one can identify for the Burgers rheology (Yuen & Peltier 1982):

$$\mu(\omega) = \frac{\mu_1 i\omega\left(i\omega + \frac{\mu_2}{\eta_2}\right)}{\left(i\omega + \frac{\mu_1}{\eta_1}\right)\left(i\omega + \frac{\mu_2}{\eta_2}\right) + \frac{\mu_1}{\eta_2}i\omega}. \tag{A4}$$

$$\lambda(\omega) = \frac{\left(\lambda_1 i\omega + \kappa\frac{\mu_1}{\eta_1}\right)\left(i\omega + \frac{\mu_2}{\eta_2}\right) + \kappa\frac{\mu_1}{\eta_2}i\omega}{\left(i\omega + \frac{\mu_1}{\eta_1}\right)\left(i\omega + \frac{\mu_2}{\eta_2}\right) + \frac{\mu_1}{\eta_2}i\omega}. \tag{A5}$$

A1.2 Gravito-viscoelastic deformations

Following Peltier (1974) we combine time-dependent love numbers $h_l(t)$ and $k_l(t)$ (where l is the spherical harmonic degree), bearing information about the Earth rheology, with the gravitational potential

of the load $S_l^m(t)$ to calculate the radial surface deformation ${u_r}_l^m(t)$ and change in gravitational potential $\Phi_l^m(t)$:

$$ {u_r}_l^m(t) = \frac{h_l(t)}{g_0} * S_l^m(t), \tag{A6} $$

$$ \Phi_l^m(t) = (\delta(t) + k_l(t)) * S_l^m(t), \tag{A7} $$

with $*$ the temporal convolution product and l, m the spherical harmonics degree and order. In our calculation, we calculate deformations on a 180×360 spatial grid, yielding a maximum spherical harmonic degree of 89, according to the Nyquist–Shannon sampling theorem, and we include the spherical harmonic degree one. We use a time step of 0.5 kyr. Taking (A6) and (A7) into Fourier domain results in a scalar product between source and Love numbers :

$$ {u_r}_l^m(\omega) = \frac{h_l(\omega)}{g_0} S_l^m(\omega), \tag{A8} $$

$$ \Phi_l^m(\omega) = (1 + k_l(\omega))\, S_l^m(\omega). \tag{A9} $$

Instead of calculating viscoelastic normal modes, we calculate $h^l(\omega)$ and $k^l(\omega)$ thanks to (A1), in addition to Poisson's equation and conservation of momentum, as the system is equivalent to solving the elastic case introduced by Alterman *et al.* (1959) when inputting $\lambda(\omega)$, $\mu(\omega)$ instead of λ_1, μ_1. Note that because the discrete Fourier transform implies periodicity of the signal, we obtain the deformation caused by an infinity of glacial periods (all identical to the last cycle), and not just the last one. Apart from this fundamental difference with the normal modes approach, we ensured that our calculation was in full agreement with the benchmark by Spada *et al.* (2011a). Finally, via inverse Fourier and spherical harmonics transforms of eqs (A8) and (A9) we obtain $u_r(t, \theta, \varphi)$ and $\Phi(t, \theta, \varphi)$.

A1.3 Sea level

The goal of this section is to explain how we can calculate the sea level function. We need this function first to obtain the total loading function (comprising both ice loading and sea level loading), and second to be able to compare the model predictions with the palaeo sea level data, in the inverse process. It is calculated from the ice loading function, present-day topography (and bathymetry), and GIA deformations (vertical displacement and geoid perturbation). We use a classical approach, similar to Farrell & Clark (1976).

Few observables are available to constrain GIA. While present-day GPS and satellite gravimetry can be used to constrain a pattern of the response, in order to provide a good constrain over time-dependent parameters (e.g. viscous rheology), one needs a time-dependent data set. Such information exist in the form of geological records of the sea level, which include, among other, former coral colonies, raised beaches, fossils of species that used to live near the shore and coastal deposits. What we label sea level here is a quantity that describes the local water thickness, that is, the difference between oceanic surface and ground elevations. Thus, our first step consists in writing the elevation of a ground point above the local sea surface:

$$ r_{\text{ground}}(t, \theta, \varphi) = T(\theta, \varphi) + u_r(t, \theta, \varphi) - \frac{\Phi(t, \theta, \varphi)}{g_0} - \xi(t), \tag{A10} $$

where ξ is the eustatic sea level, that is, the mean water thickness over oceans, and T the present-day bathymetry or topography (Amante & Eakins 2009). Fig. A1 illustrates the different components used in the r_{ground} expression.

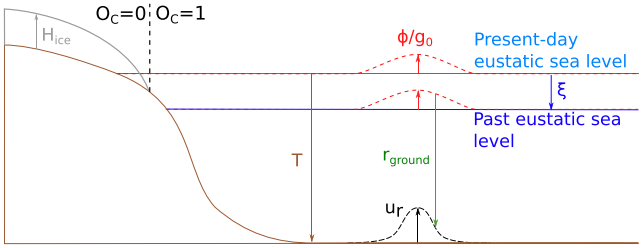

Figure A1. Schematic of the sea level components. All quantities are counted positively upwards.

The sea level can then be expressed as the opposite of ground elevation where it is negative, and 0 elsewhere:

$$ H_{\text{water}}(t, \theta, \varphi) = -r_{\text{ground}}(t, \theta, \varphi)\; O_C(t, \theta, \varphi), \tag{A11} $$

with O_C a mask function, called the ocean-continent function, equal to 1 on oceanic locations and 0 elsewhere:

$$ O_C(t, \theta, \varphi) = \begin{cases} 1, & \text{if } r_{\text{ground}}(t, \theta, \varphi) + H_{\text{ice}}(t, \theta, \varphi) < 0 \\ 0, & \text{otherwise} \end{cases}, \tag{A12} $$

and $H_{\text{ice}}(t, \theta, \varphi)$ the ice thickness expressed as equivalent oceanic water thickness.

We define u_r, Φ and ξ as the difference between past and present-day states, that is, $u_r(t = 0, \theta, \varphi)$, $\Phi(t = 0, \theta, \varphi)$, and $\xi(t = 0) = 0$ for any θ and φ. For other quantities, let Δ mark the difference between a given state and present-day state, so for a quantity Q, $\Delta Q = Q(t) - Q(t = 0)$. For H_{water} it yields:

$$ \Delta H_{\text{water}}(t, \theta, \varphi) = H_{\text{water}}(t, \theta, \varphi) - H_{\text{water}}(t = 0, \theta, \varphi) \tag{A13} $$

$$ \Delta H_{\text{water}} = -O_C(t) \left(T + u_r - \frac{\Phi}{g_0} - \xi \right) + O_C(t = 0)\; T \tag{A14} $$

$$ \Delta H_{\text{water}} = -\Delta O_C\; T + O_C \left(\frac{\Phi}{g_0} - u_r + \xi \right), \tag{A15} $$

The total load is the sum of oceanic load and ice load:

$$ H(t, \theta, \varphi) = H_{\text{water}}\; O_C + H_{\text{ice}}\; (1 - O_C) \tag{A16} $$

$$ \Delta H(t, \theta, \varphi) = \Delta H_{\text{water}}\; O_C + \Delta H_{\text{ice}}\; (1 - O_C). \tag{A17} $$

Note that where $O_C = 1$ and $H_{\text{ice}} \neq 0$, there is both ice and ocean: this happens on locations where the ice weight is not high enough to reach the bottom of the ocean. In such cases it becomes floating ice (i.e. isostatically compensated), which does not generate any GIA deformation. It is basically equivalent to a location with only oceanic liquid water. In order to conserve the water mass balance, one needs the following at any time:

$$ \int_{S_{\text{Earth}}} \Delta H \; \mathrm{d}S = 0 \tag{A18} $$

$$ \int_{S_{\text{Earth}}} \left[T \Delta O_C - O_C \left(\frac{\Phi}{g_0} + \xi - u_r \right) \right] \mathrm{d}S = \int_{S_{\text{Earth}}} \Delta H_{\text{ice}} (1 - O_C)\; \mathrm{d}S, \tag{A19} $$

$$\int_{S_{\text{Earth}}} -O_C \xi \, \mathrm{d}S = \int_{S_{\text{Earth}}} \Big[-T\Delta O_C + O_C \left(\frac{\Phi}{g_0} - u_r \right) + \Delta H_{\text{ice}}(1 - O_C) \Big] \mathrm{d}S, \tag{A20}$$

where $\mathrm{d}S$ is a spherical surface element. As ξ is only time-dependent and $\int_{S_{\text{Earth}}} O_C = S_{\text{ocean}}$, the condition for mass balance becomes:

$$\xi = \frac{1}{S_{\text{ocean}}} \int_{S_{\text{Earth}}} \left[T\Delta O_C + O_C \left(u_r - \frac{\Phi}{g_0} \right) - \Delta H_{\text{ice}}(1 - O_C) \right] \mathrm{d}S. \tag{A21}$$

We thus know every term in the total loading expression, built from eqs (A15) and (A17):

$$\Delta H(t, \theta, \varphi) = -\Delta O_C \; T + O_C \left(\frac{\Phi}{g_0} - u_r + \xi \right) + (1 - O_C)\Delta H_{\text{ice}}. \tag{A22}$$

For direct problems, one can easily solve the total sea level equation expressed by eqs (A13)–(A22). However, in order to reduce the dimensionality of the Bayesian inversion so that it can converge faster and more easily, the ice coefficients are inverted by a linear least-squares method. This represents a simplification compared to some of the advances since by (Johnston 1993; Milne & Mitrovica 1998; Lambeck *et al.* 2003) as the method implemented is close to the original theory of Farrell & Clark (1976). The linear least-squares method requires to preserve the linearity of the response with respect to the source, so we have to neglect the variation of the ocean-continent function with time, which causes $T\Delta O_c$ to vanish and the other terms to be only slightly perturbed. We chose O_C such that :

$$O_C(\theta, \varphi) = \begin{cases} 1, \text{ where } T(\theta, \varphi) < 0, \text{ and } H_{\text{ice}}(t, \theta, \varphi) = 0 \; \forall t \\ 0 \text{ otherwise} \end{cases}. \tag{A23}$$

Finally, the expression for the linearized loading is:

$$\Delta H(t, \theta, \varphi) = O_C(\theta, \varphi) \left(\frac{\Phi(t, \theta, \varphi)}{g_0} - u_r(t, \theta, \varphi) + \xi(t) \right) + (1 - O_C(\theta, \varphi))\Delta H_{\text{ice}}(t, \theta, \varphi). \tag{A24}$$

In the initial state we input the charge such that :

$$\Delta H = (1 - O_C)\Delta H_{\text{ice}} + \frac{O_C}{S_{\text{ocean}}} \int_{S_{\text{Earth}}} -\Delta H_{\text{ice}}(1 - O_C) \mathrm{d}S. \tag{A25}$$

We then iterate eqs (A8) and (A9), along with the rotational feedback signal, to calculate deformation, then eq. (A24) recalculates the charge and sea level response, until the convergence reaches a threshold in the sea level response of 0.1 m RMS difference between two iterations.

We addressed the impact of our linearization approximation in two ways. First, with a forward model approach, we investigated whether there were areas or epochs subject to errors. For this purpose, we compared the response with full sea level resolution using (A22) and the response neglecting the change of O_C with time, and found that the differences are very small (less than 1 m in the early phase of the deglaciation and significantly less towards the present-day) except in the Barents sea region where a large area emerges around the LGM and gets flooded again in the late cycle. In this region the difference can reach several tens of metres. We are however confident that this did not affect our inversion as we do not use any sea level record from this region. Second, we assessed the potential bias created by an incorrect oceanic surface ratio. Our ocean-continent function is fixed, with a geometry where the oceanic surface is minimum (resembling the near-LGM situation) so that all the ice introduced in the reference model generates GIA signal (even in region flooded later during the cycle such as the Barrents Sea). In this situation the ocean covers about 68.8 per cent of the Earth, while the maximum coverage during the cycle should be around 70.8 per cent, so we are overestimating our sea level predictions with the reference model between 0 per cent and $1 - 0.688/0.708 = 3.05$ per cent. We thus expect this approximation to lead to a relative underestimate of the alpha coefficients and LGM eustatic sea level (derived from the alpha coefficients and spatial integration of the reference model) by a maximum of $\sim$3 per cent. This should of course be addressed in our future investigations, but nevertheless, given the uncertainties affecting the ice parameters we think that this does not cause any significant change in our conclusions.

A2 Inverse methods : Bayesian Monte Carlo with Markov chains

Inversion is the process by which one can get information from the observables on the parameters. In a Bayesian framework, the concept is to attribute a probability value to any given forward model, which corresponds to the probability that, among all tested models, it is the right model to represent the physical phenomenon.

The principle of Monte Carlo methods is to test a large group of forward models, exploring the parameters space, and compare their predictions to the observed data. Since it is a trial-and-error method, it allows for inverting non-linear physics, which is the case of viscoelastic rheology. For this reason, the parameters inverted by Monte Carlo methods in our inversion are $\eta_{1\text{UM}}$, $\eta_{1\text{LM}}$, T_e, μ_1/μ_2 and $10^{\eta_1}/10^{\eta_2}$.

Let $\boldsymbol{x}$ be the parameters vector, and $\boldsymbol{y}$ the data vector. We want to get the probability distribution of the parameters given the data set, written $p(\boldsymbol{x}|\boldsymbol{y})$ and called *a posteriori* probability. Bayes rule states that:

$$p(\boldsymbol{x}|\boldsymbol{y}) = \frac{p(\boldsymbol{y}|\boldsymbol{x})p(\boldsymbol{x})}{K_1}, \tag{A26}$$

where K_1 is a constant that ensures that $\int p(\boldsymbol{x}|\boldsymbol{y})\mathrm{d}\boldsymbol{x} = 1$. $p(\boldsymbol{x})$ is called the *a priori* distribution of the parameters, and contains information we have on the parameters before the inversion. In our work, it is set to be a rectangular function, that is, it adds no information but the range of values in which we pick the parameters. $p(\boldsymbol{y}|\boldsymbol{x})$ is called the likelihood function, and contains the information acquired during the inversion. On its basic form, assuming a L2-norm, it is a Gaussian distribution whose mean is the data $\boldsymbol{y}$, standard deviation is the data uncertainty $\boldsymbol{\epsilon}$ and variable is the model prediction $\boldsymbol{y^m}$:

$$p(\boldsymbol{y}|\boldsymbol{x}) = \exp\left(-\sum_{i=1}^{N_{\text{data}}} \frac{1}{2} \left(\frac{\boldsymbol{y}_i^m(\boldsymbol{x}) - \boldsymbol{y}_i^d}{\epsilon_i} \right)^2 \right). \tag{A27}$$

In this form, the importance of each observation is weighted solely by its measurement uncertainty, however in geophysical data sets one common problem is that the data can be very unevenly distributed in time and space, which, for example, can lead the inversion to give better probability to models fitting well a small area with high data density and poorly the rest of the world. To compensate this effect we introduced a weight $\boldsymbol{w}$ that accounts for

redundant information in the data set. This weight was obtained by exploring the parameter space in a first Monte Carlo search and noting which predictions were typically correlated. If two or more predictions are typically correlated no matter what the parameters values are, then their information on the parameters is somewhat redundant. In our case, this is often the case when these data are close in space and/or time. Hence, the weight of the ith data can be expressed as:

$$w_i = \frac{K_2}{\sum_{j=1}^{N_{\text{data}}} \text{corr}(y_i^m, y_j^m)}, \tag{A28}$$

where $\text{corr}(y_i^m, y_j^m)$ is the linear correlation coefficient between y_i^m and y_j^m over all models sampled and K_2 is a constant that ensures that the mean weight is 1, so as not to bias the statistics. In our inversion, we calculate this coefficient for both Burgers and Maxwell rheologies and find that less than 5 per cent of the data bears a different amount of information depending on the rheological model (i.e. the mean difference in correlation coefficient was larger than 0.1). Hence, we choose to use the same weights in those two cases. The robustness of these coefficients was tested by a bootstrap algorithm to see if the number of sample models in the parameter space was large enough, and we found that differences in the correlation coefficients do not exceed 10^{-3}. Finally, the most weighted data to least weighted data ratio is less than 4, so we are confident that we are not biasing the result by over weighting. The likelihood then becomes:

$$p(\boldsymbol{y}|\boldsymbol{x}) = \exp\left(-\sum_{i=1}^{N_{\text{data}}} \frac{{w_i}^2}{2}\left(\frac{y_i^m(\boldsymbol{x}) - y_i^d}{\epsilon_i}\right)^2\right). \tag{A29}$$

In this form, the likelihood accounts for the data uncertainty and spatiotemporal distribution, however we found that the spread of the predictions was still much larger than what the data uncertainty would predict. Such gaps between data and predictions are probably due to the model being only an approximation of the real structure and rheology of the mantle and real ice loading function, not mentioning other possible sources of error such as linearization of the equations and the iterative methods for solving the sea level equation. Furthermore, it is difficult to rule out any possibility that the data contains some non-GIA signal (e.g. a tectonic component), which will not be accounted by the measurement uncertainty either. Unfortunately, there is no way to account for all of these sources of discrepancy, and the former expression of the likelihood would lead to very high differences in probability for very similar models, due to its exponential nature. An ad hoc way to go around this problem is to normalize the misfit to the standard deviation of the data, yielding:

$$p(\boldsymbol{y}|\boldsymbol{x}) = \exp\left(-\sum_{i=1}^{N_{\text{data}}} \frac{{w_i}^2}{2\sigma_{\text{dataset}}^2}\left(\frac{y_i^m(\boldsymbol{x}) - y_i^d}{\epsilon_i}\right)^2\right). \tag{A30}$$

We used the Simulated Annealing algorithm (Kirkpatrick *et al.* 1983), a variation of the Monte Carlo with Markov chains method (Metropolis & Ulam 1949; Metropolis *et al.* 1953), to perform model sampling, which consists of the following:

(i) Initialize first model with random parameters $\boldsymbol{x^1}$ and calculate its *a posteriori* probability p^1. Mark this model as the last accepted model, $\#l_a$. Initialize the so-called 'temperature' value $\text{Temp} = \text{Temp}_{\text{max}}$ (term originated from the development of the simulated annealing technique in metallurgy).

(ii) Generate a new model $\#i$ in the vicinity of the last accepted model: $\boldsymbol{x^i} = \boldsymbol{x^{l_a}} + \boldsymbol{a\delta x}$, with a a vector with values $\in [-0.5, 0.5]$. We let $\boldsymbol{\delta x}$ decrease as the number of models increase to allow convergence to a better precision.

(iii) If $b \leq (\frac{p^i}{p^{l_a}})^{\frac{1}{\text{Temp}}}$ then update $l_a := i$, with b a random number $\in [0, 1]$. Decrease temperature multiplying Temp by a factor $1 - \epsilon$, with $\epsilon \ll 1$.

(iv) Repeat steps (ii) and (iii) until the desired number of models has been reached.

This method provides a good compromise between exploring the whole parameters space when 'Temp' is high (i.e. the acceptance probability $(\frac{p^i}{p^{l_a}})^{\frac{1}{\text{Temp}}}$ always close to 1), and focusing on the part of the space where the probability is non-negligible, thus providing better convergence around the probability maxima, when 'Temp' is low. Note that this method decreases the risk to get stuck in a local maximum compared to other methods, such as the Metropolis algorithm.

A3 Inversion results

In this section we present all probability maps derived from our inversions. Figs A2–A4 represent the results of the inversions with the ANU ice history model as reference, respectively with Maxwell rheology, Burgers rheology when fixing $\mu_1/\mu_2 = 5$ and $10^{\eta_1}/10^{\eta_2} = 5$, and Burgers rheology with μ_1/μ_2 and $10^{\eta_1}/10^{\eta_2}$ as parameters included in the inversion. Figs A5–A7 represent similarly the results with the ICE-5G model as reference for ice history. In addition to the observations made in Section 3, let us remark that the ice coefficients are always highly correlated, and not necessarily in a linear way. The least-squares matrix provided by our method evidenced that this correlation is almost non-existent with a fixed rheology, so this trade-off effect originates from the correlation between ice coefficients and rheology parameters, particularly the lower-mantle viscosity rather than an intrinsic correlation between ice coefficients. There is, however, an exception for the correlation between ice in Antarctica and Greenland, which can reach a moderate value of about 0.4, due to the role of these ice sheets in adjusting the far-field sea level in our data set. When looking at the probability maps for μ_1/μ_2 and $10^{\eta_1}/10^{\eta_2}$ in the ANU case, we notice that we cannot constrain a best value for these parameters. Indeed, since when μ_1/μ_2 or $10^{\eta_1}/10^{\eta_2}$ is small the contribution of the Kelvin–Voigt element is negligible, many Burgers models behave like Maxwell models, and we found that the probability in the Burgers rheology can reach about the same maximum value as in the Maxwell case, so we cannot constrain any minimum value of these parameters. Because of this effect, we cannot constrain any maximum value either, because there is always a part of the space parameters where the other ratio makes the Kelvin–Voigt contribution vanish, and the model behaves like a Maxwell rheology. The only case where the Burgers ratio would cause the fit to drop is the case where both are very high (i.e. greater than 10). Hence, in the case with fixed ratio for Burgers rheology, we choose a value of 5 that still provides a good fit while having a non-negligible Kelvin–Voigt contribution. It seems however that values around $\mu_1/\mu_2 = 10$ and $10^{\eta_1}/10^{\eta_2} = 3$ allow to increase the long-term upper-mantle viscosity to 10^{21} Pa s without lowering the probability significantly. Furthermore, it even yields the best fit that we could achieve in the ICE-5G case, so while we find that the Burgers rheology only influences the long wavelengths and thus interacts only with the lower-mantle viscosity in general, it seems possible to find Burgers parameters that influence the upper-mantle viscosity.

Our approach has several weak points which could be improved in the future. First, we use a spherical Earth model with no lateral

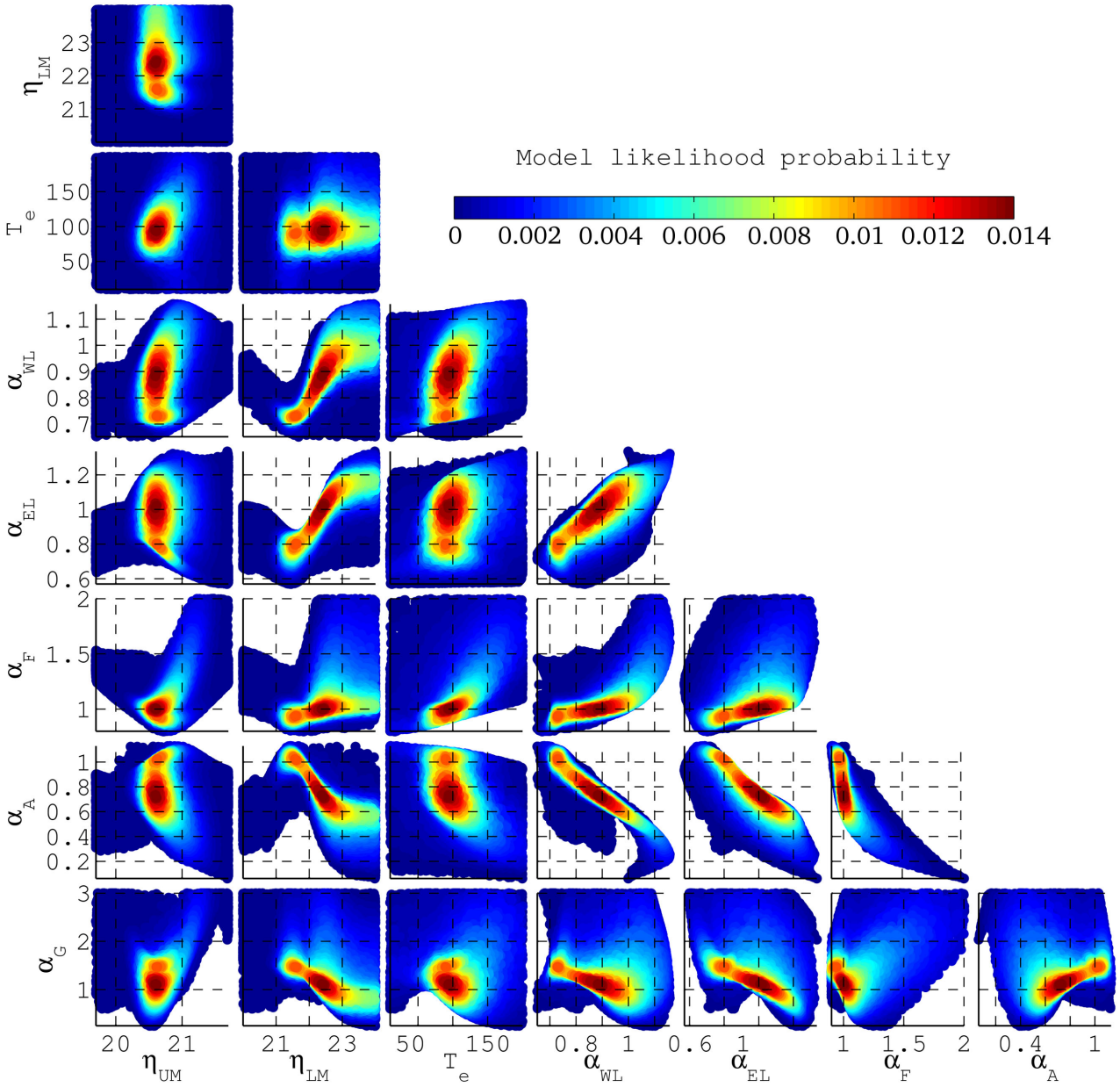

Figure A2. *A posteriori* probability distribution projected on the 2-D space formed by each pair of parameters in the ANU-based Maxwell inversion. Note that models with larger probability are plotted on top of lower probability models.

variations, which yields results probably more representative of the Laurentia and Fennoscandia cratonic regions, where the main sources of signal and the larger portion of the sea level data are located. This could lead to a bias in the prediction of the far-field data, in oceanic regions characterized by a thinner lithosphere and a less viscous upper mantle, as evidenced by Lambeck *et al.* (2014). A similar bias may apply to other non-cratonic areas which are closer to the ice load, such as the British Isles and west Antarctica.

Second, resolving the ice coefficients by linear least squares leads us to linearize the sea-level equation with respect to the ice loading, which, as discussed in Appendix A1.3, could introduce errors in present-day flooded areas that were above sea level sometime during the glacial cycle, for example, the Barents sea region. Finally, we used only sea level data to constrain the inversion, but other data sets such as GPS, geoid rate, gravity gradients and other geodetic data, etc., could provide further constraints over the parameters.

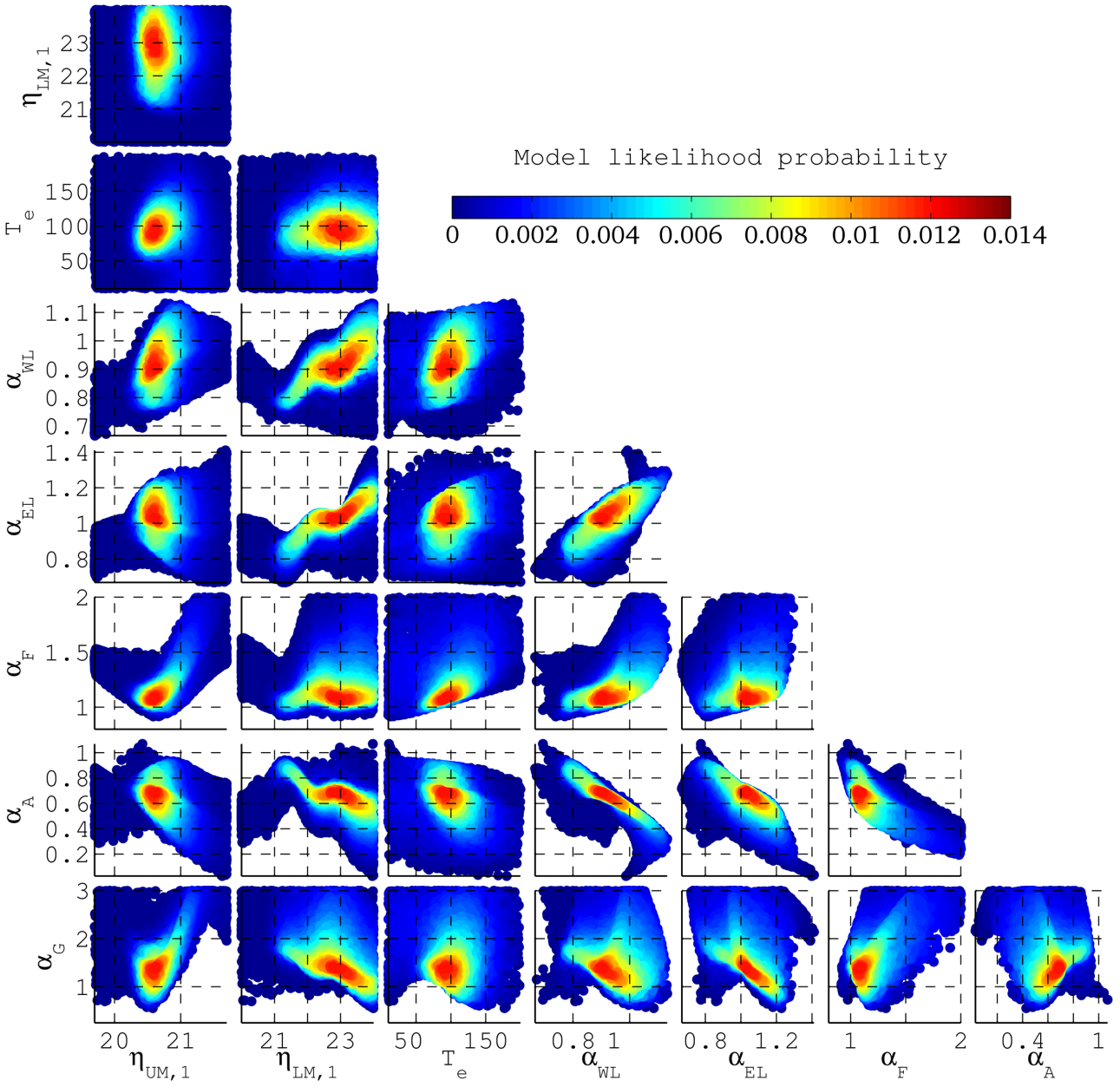

Figure A3. *A posteriori* probability distribution projected on the 2-D space formed by each pair of parameters in the ANU-based Burgers inversion, with $\mu_1/\mu_2 = 5$ and $10^{\eta_1}/10^{\eta_2} = 5$. Note that models with larger probability are plotted on top of lower probability models.

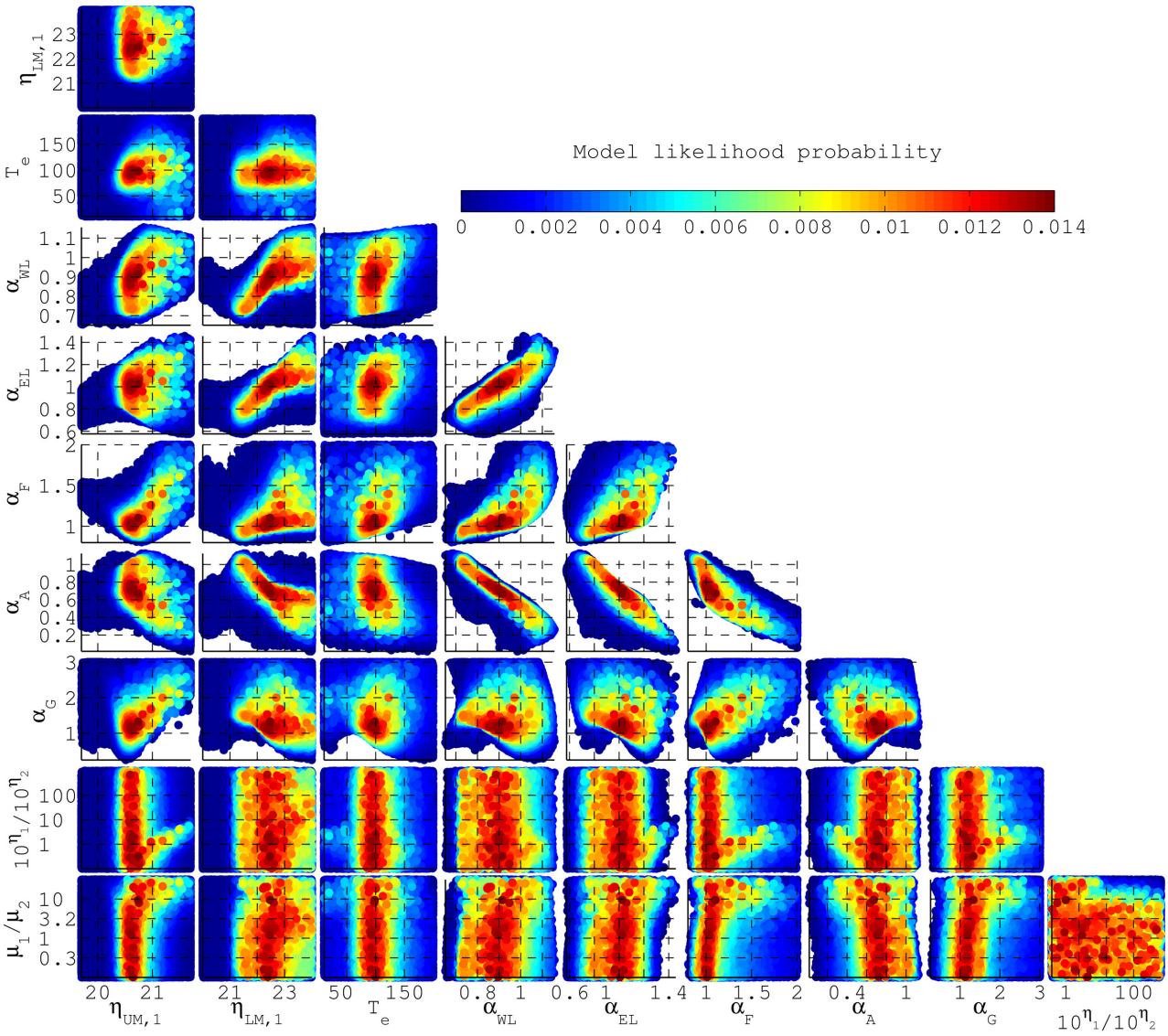

Figure A4. *A posteriori* probability distribution projected on the 2-D space formed by each pair of parameters in the ANU-based Burgers inversion. Note that models with larger probability are plotted on top of lower probability models.

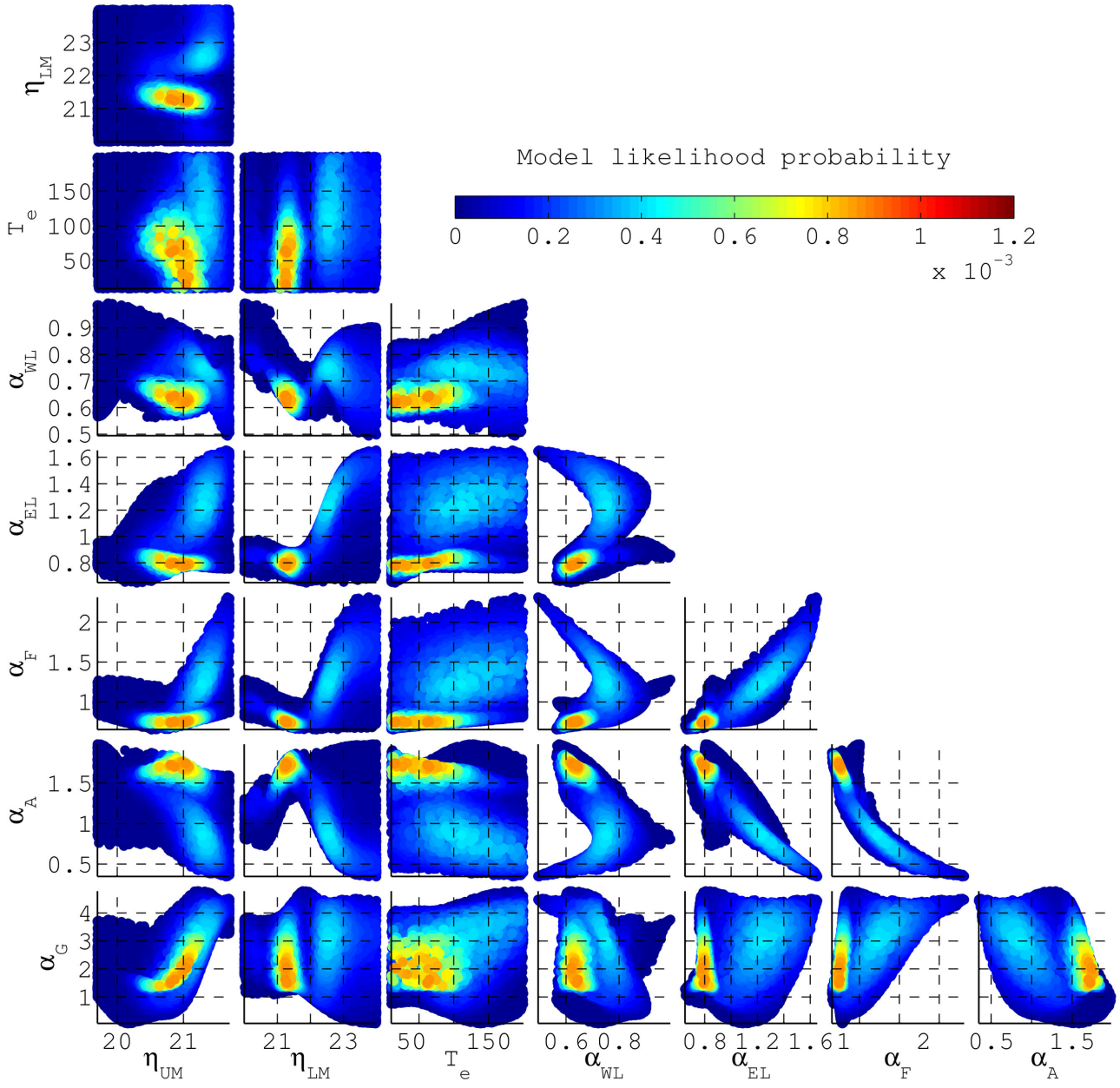

Figure A5. *A posteriori* probability distribution projected on the 2-D space formed by each pair of parameters in the ICE-5G-based Maxwell inversion. Note that models with larger probability are plotted on top of lower probability models.

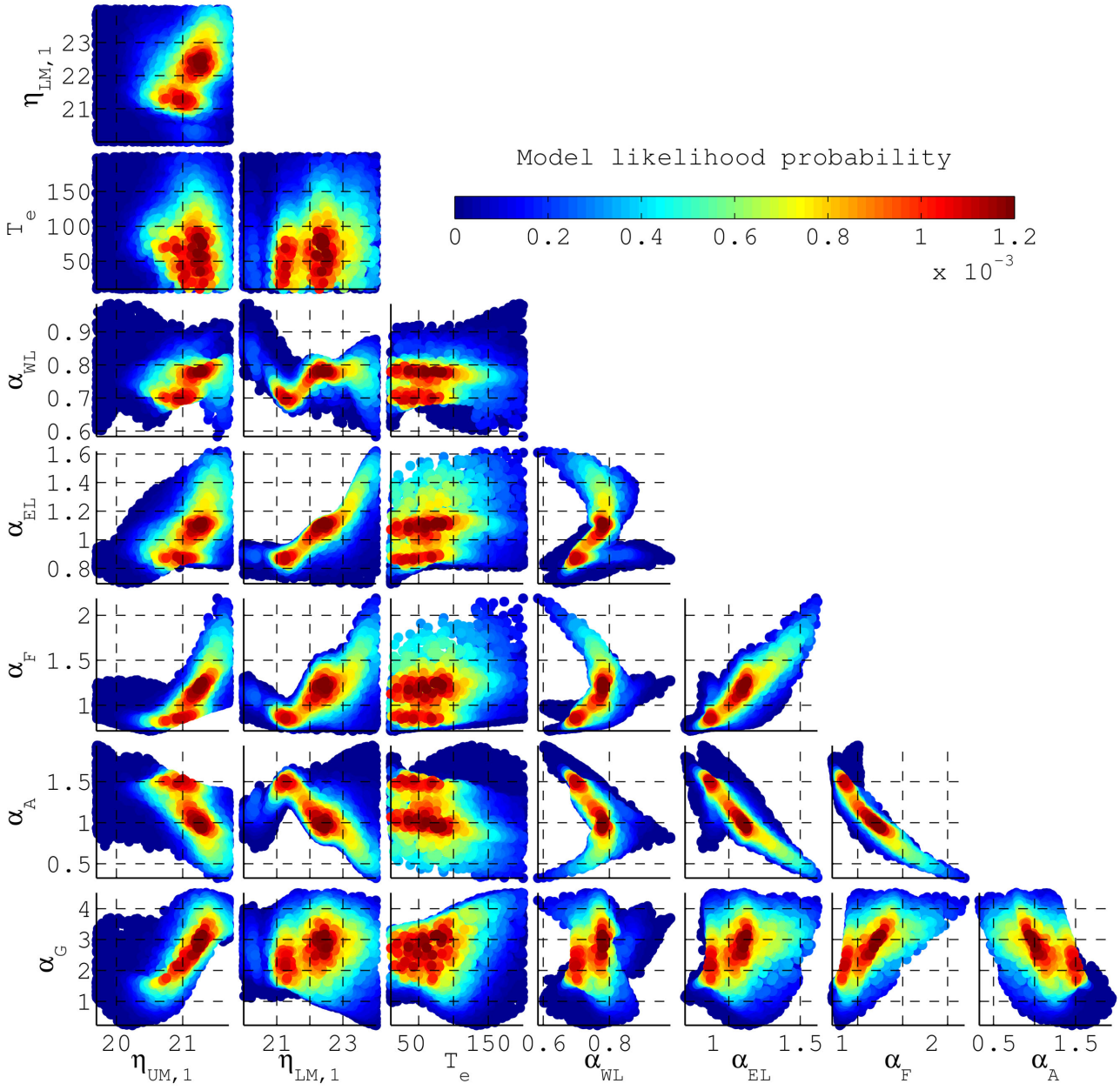

Figure A6. *A posteriori* probability distribution projected on the 2-D space formed by each pair of parameters in the ICE-5G-based Burgers inversion, with $\mu_1/\mu_2 = 5$ and $10^{\eta_1}/10^{\eta_2} = 5$. Note that models with larger probability are plotted on top of lower probability models.

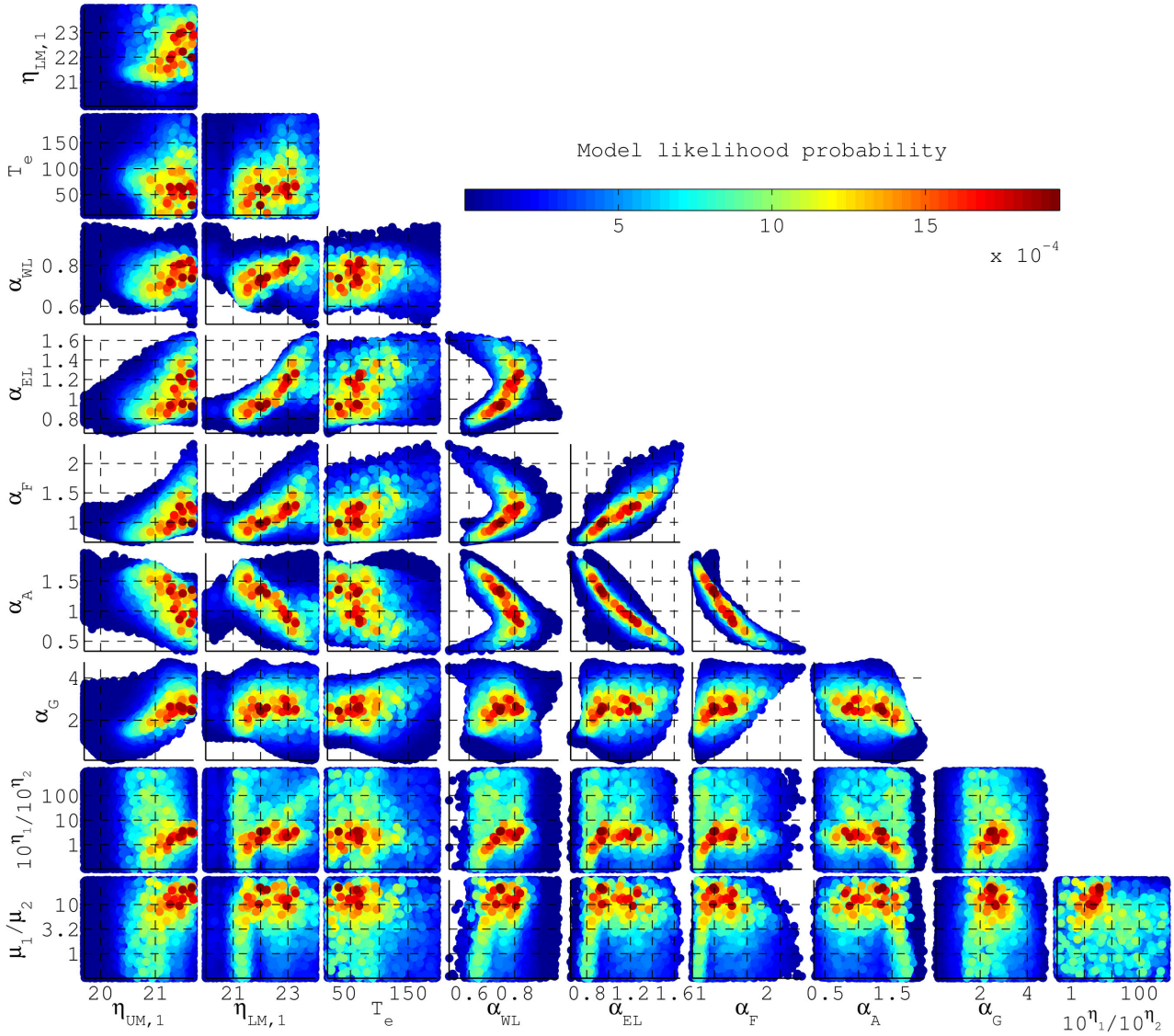

Figure A7. *A posteriori* probability distribution projected on the 2-D space formed by each pair of parameters in the ICE-5G-based Burgers inversion. Note that models with larger probability are plotted on top of lower probability models, and that the colour scale is different from Figs A5 and A6.